

# Controlling field asymmetry in nanoscale gaps for second harmonic generation

Jessica Meier,<sup>†,¶</sup> Luka Zurak,<sup>†,¶</sup> Andrea Locatelli,<sup>‡</sup> Thorsten Feichtner,<sup>†</sup> René Kulloock,<sup>†</sup> and Bert Hecht<sup>\*,†</sup>

<sup>†</sup>*Nano-Optics and Biophotonics Group, Experimental Physics 5, Institute of Physics, University of Würzburg, Germany*

<sup>‡</sup>*Department of Information Engineering, University of Brescia, Italy*

<sup>¶</sup>*These authors contributed equally*

E-mail: hecht@physik.uni-wuerzburg.de

## Abstract

Plasmonic dimer antennas create strong field enhancement by squeezing light into a nanoscale gap. These optical hotspots are highly attractive for boosting nonlinear processes, such as harmonic generation, photoelectron emission, and ultrafast electron transport. Alongside large field enhancement, such phenomena often require control over the field asymmetry in the hotspot, which is challenging considering the nanometer length scales. Here, by means of strongly enhanced second harmonic generation, we demonstrate unprecedented control over the field distribution in a hotspot by systematically introducing geometrical asymmetry to the antenna gap. We use focused helium ion beam milling of mono-crystalline gold to realize asymmetric-gap dimer antennas in which an ultra-sharp tip with 3 nm apex radius faces a flat counterpart, conserving the bonding antenna mode and the concomitant field enhancement at the fundamental frequency. By decreasing the tip opening angle, we are able to systematically increase

both field enhancement and asymmetry, thus enhancing second harmonic radiation to the far-field, which is nearly completely suppressed for equivalent symmetric dimer antennas. Combining these findings with second harmonic radiation patterns as well as quantitative nonlinear simulations, we further obtain remarkably detailed insights into the mechanism of second harmonic generation at the nanoscale. Our results open new opportunities for the realization of novel nonlinear nanoscale systems, where the control over local field asymmetry in combination with large field enhancement is essential to create nonreciprocal functionalities.

## Keywords

second-harmonic generation, local field asymmetry, local symmetry breaking, nonlinear plasmonics, helium ion beam milling, nanoscale gaps

## Introduction

Plasmonic nanostructures allow to squeeze light into nanoscale volumes providing strong field hotspots that can significantly enhance nonlinear effects.<sup>1,2</sup> A variety of such processes not only require high field enhancement, but also control over the symmetry of the field distribution. This includes even-order harmonic generation,<sup>3</sup> directed electron transport,<sup>4,5</sup> optical rectification,<sup>6-8</sup> and photoelectron emission.<sup>9-11</sup> For the latter, asymmetry was geometrically imposed, however, using rather large feature sizes ( $> 20$  nm), which provide field asymmetry only at the expense of drastically reduced field enhancement. On the sub-10 nm scale, controlling field asymmetry is extremely challenging, and is typically randomly generated as in electromigrated gaps.<sup>12,13</sup> Another means to break the field symmetry in a nanoscale gap are asymmetric few-cycle phase-stable laser pulses,<sup>4,5</sup> which offer some flexibility but are experimentally challenging.

Second harmonic generation (SHG) is a phenomenon that is especially sensitive to both

field enhancement and asymmetry. For centrosymmetric materials such as gold, it only occurs at metal-dielectric interfaces where the symmetry is broken.<sup>14,15</sup> However, even though symmetric plasmonic dimer antennas with nanometer-sized gaps feature among the largest reported field enhancements for bonding mode resonances,<sup>16,17</sup> typically axial or inversion symmetry in the overall geometry of nanostructures leads to destructive interference of the resulting SH radiation in the far-field.<sup>18,19</sup> Recent work has addressed this so-called silencing effect by breaking the *global* symmetry of either the structure geometry<sup>20-24</sup> or by employing light-induced symmetry breaking.<sup>25</sup> In addition, in some experiments a resonance at the SH was achieved.<sup>26-30</sup> However, in all these cases the lack of global symmetry considerably reduces the field enhancement.

Here, we demonstrate controlled *local* symmetry breaking of the field distribution in a sub-10 nm gap of a plasmonic dimer antenna, while preserving the bonding mode at the fundamental frequency, which is responsible for the large field enhancement. Unprecedented control over the gap geometry is achieved using helium-based focused ion beam milling (He-FIB) of mono-crystalline gold microplatelets. We realize asymmetric-gap antennas featuring ultra-sharp tips with a tip apex radius down to 3 nm for a gap size of 8 nm, where the degree of asymmetry can be directly controlled by modifying the tip opening angle. Local symmetry breaking leads to an asymmetric SH surface polarization in the gap, which efficiently radiates into the far-field with a nonlinear coefficient of up to  $\gamma_{\text{SH}} = 1.7 \times 10^{-10} \text{ W}^{-1}$ . Importantly, our approach retains the full geometric freedom afforded by in-plane antenna structures. We are thus able to record SH radiation as a function of the degree of local asymmetry, and, above that, to compare a large number of asymmetric-gap antennas to their symmetric counterparts with equal bonding mode resonances. By further recording SH radiation patterns we infer a quantitative description of the microscopic origin of SHG, which confirms the experimentally achieved large degree of asymmetry of the field distribution in the antenna hotspot.

# Results and discussion

## Concept of local symmetry breaking

The emission of SH radiation by a plasmonic nanoantenna to the far-field is described by the total SH polarization

$$\mathbf{P}^{(2\omega)} = \mathbf{P}_S^{(2\omega)} + \mathbf{P}_R^{(2\omega)}, \quad (1)$$

where  $\mathbf{P}_R^{(2\omega)}$  denotes the response polarization of the antenna at the SH frequency driven by the SH source  $\mathbf{P}_S^{(2\omega)}$ . For centrosymmetric materials, such as gold,  $\mathbf{P}_S^{(2\omega)}$  is a pure surface polarization, which is approximated as (see also Supplementary Section 1.3):

$$\mathbf{P}_S^{(2\omega)}(\mathbf{r}) = \epsilon_0 \chi_{S,\perp,\perp,\perp}^{(2)} E_{\perp}^{(\omega)}(\mathbf{r}) E_{\perp}^{(\omega)}(\mathbf{r}) \hat{r}_{\perp} \delta(\mathbf{r} - \mathbf{r}_S), \quad (2)$$

where  $\chi_{S,\perp,\perp,\perp}^{(2)}$  is the dominant component of the  $\bar{\bar{\chi}}_S^{(2)}$  tensor,  $E_{\perp}^{(\omega)}$  is the normal component of electric field at the metal surface at frequency  $\omega$ ,  $\mathbf{r}_S$  denotes a position vector pointing at the surface, and  $\hat{r}_{\perp}$  is the surface unit normal vector.<sup>31–33</sup>

For a mirror-symmetric plasmonic dimer antenna with nanometer-sized gap, dipolar SH radiation is expected to cancel due to the silencing effect,<sup>18,19</sup> despite the strong field enhancement in the gap at the fundamental frequency (FF) (see Fig. 1a and b). The silencing effect for such a symmetric-gap antenna becomes apparent when analyzing the SH polarization as displayed in Fig. 1c, showing both contributions, *i.e.*  $\mathbf{P}_S^{(2\omega)}$  (black arrows) and  $\mathbf{P}_R^{(2\omega)}$  (grey arrows), obtained from nonlinear simulations that will be introduced later. Integrating the nonlinear polarization over each antenna arm yields effective SH dipole moments, represented by the large purple and orange arrows for the left and right antenna arm, respectively. As these effective SH dipoles oscillate out-of-phase, SH radiation interferes destructively in



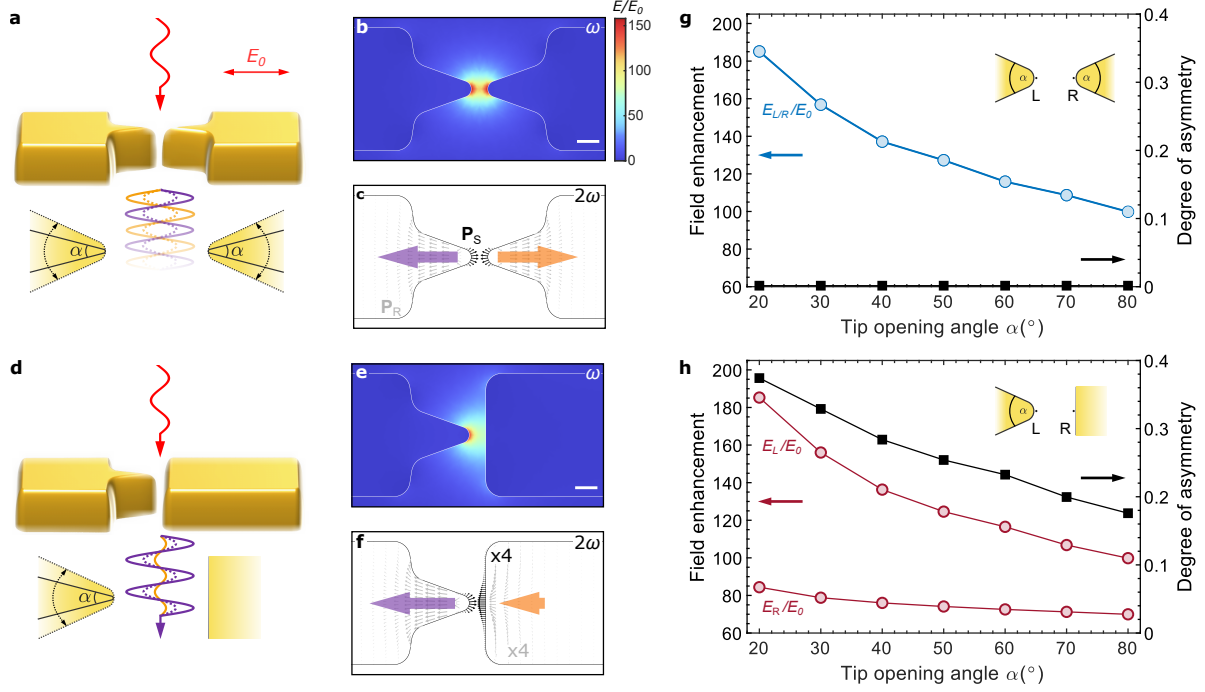


Figure 1: **Effect of local symmetry breaking on the SHG process in gold nanoantennas.** Upon excitation with a linear polarized laser at frequency  $\omega$ , the SH efficiency depends on the gap geometry. **a**, Symmetric-gap antenna. The SH response at  $2\omega$  can be described by two out-of-phase oscillating effective dipoles of equal amplitude originating at the tips of the left (purple) and right (orange) antenna rod. **b**, Simulated linear field enhancement plot evaluated around the gap region (cut parallel to the substrate at half of the antenna height) at the resonance frequency of the global bonding antenna mode. **c**, Real part of simulated second-order polarization  $\mathbf{P}^{(2)}$ , consisting of source polarization  $\mathbf{P}_S^{(2)}$  (black arrows) and response polarization  $\mathbf{P}_R^{(2)}$  (grey arrows), see Eq. (1). Purple and orange arrows correspond to effective dipoles introduced in **a**. **d-f**, Asymmetric-gap antenna. The corresponding effective dipoles differ in amplitude and oscillate in-phase. The SH signal can be tuned by modifying the tip opening angle (see dashed line in the lower panel of **d**). **g,h**, Field enhancement evaluated 0.1 nm from the surface at positions L/R (see inset) for symmetric-gap (blue) and asymmetric-gap (red) antenna, respectively. Black square symbols correspond to the degree of asymmetry, see Eq. (3). Scale bars in **b** and **e**, 10 nm.

the far-field.

The silencing effect can be overcome by breaking the local symmetry of the field distribution. To this end, we taper only one side of the gap to produce a sharp tip facing a flat counterpart (see Fig. 1d), which yields an asymmetric field enhancement at the two sides of the gap. Since symmetry is broken locally, the global symmetry of the resonant bonding antenna mode remains unaffected resulting in a field enhancement at the FF comparable to that of the symmetric-gap antenna (Fig. 1e). The asymmetric field distribution at the FF leads to an asymmetric nonlinear polarization distribution visualized in Fig. 1f, where effective dipoles no longer cancel but oscillate in-phase, leading to strong SH radiation in the far-field.

Field enhancement and field distribution in the gap strongly depend on the gap size as well as on the size of the tip apex. By keeping the gap size fixed and changing only the tip opening angle  $\alpha$ , *i.e.* the sharpness of the tip, we systematically modify the properties of the field. Fig. 1g and h display the field enhancement at the FF evaluated 0.1 nm from the left and right surface of the gap at half of the antenna height (labeled as positions L/R in the insets) for tip opening angles ranging from  $80^\circ$  down to  $20^\circ$  for symmetric-gap and asymmetric-gap antennas, respectively. For the same tip opening angles symmetric-gap and asymmetric-gap antennas exhibit an approximately equal field enhancement of about 100 for the case of  $80^\circ$ , which increases up to 185 for a tip opening angle of  $20^\circ$ . To assess the influence of field asymmetry on SHG, we define the degree of asymmetry (DOA) of the system as the contrast between field enhancements at positions L and R:

$$\text{DOA} := \frac{E_L - E_R}{E_L + E_R}. \quad (3)$$

If we assume dipole-like sources situated at the left and right side of the gap with strengths proportional to square of the field amplitudes (see Eq. 1), the expected SH power radiated

to the far-field is proportional to the square of the effective dipole and can be written as

$$P_{\text{SH}} \propto [E_{\text{L}}^2 - E_{\text{R}}^2]^2 \propto E_{\text{avg}}^4 \cdot \text{DOA}^2, \quad (4)$$

where  $E_{\text{avg}} = (E_{\text{L}} + E_{\text{R}})/2$  is the average of the field strengths to the left and to the right side of the gap. Eq. (4) highlights the importance of both field enhancement and asymmetry of the system with respect to achieving strong SHG. Although both types of antenna exhibit comparable field enhancement, the DOA is vanishing for all tip opening angles in the case of symmetric-gap antennas (black line in Fig. 1g) implying complete suppression of SHG. For asymmetric-gap antennas, however, modifying the tip opening angle allows us to separately change the field enhancement at the two sides of the gap and consequently to achieve non-zero DOA (Fig. 1h). As the tip gets sharper both field enhancement and DOA are increased, thus leading to strongly enhanced SHG.

## Fabrication and optical characterization

Realizing local symmetry breaking in plasmonic nanoantennas requires full control over the shape of the narrow gap region that can hardly be achieved even with high-end nanofabrication techniques, such as electron-beam lithography,<sup>34</sup> electromigration,<sup>13,35</sup> break junctions,<sup>36,37</sup> metal-nanoparticle assemblies,<sup>25,38,39</sup> and focused ion beam milling of mono-crystalline gold microplatelets with gallium ions (Ga-FIB).<sup>40</sup> He-FIB of evaporated gold films already surpasses pure Ga-FIB and reaches sub-10 nm precision.<sup>41</sup> However, the combination of He-FIB with mono-crystalline gold microplatelets, results in even smaller feature sizes leading to an unprecedented fabrication accuracy and reproducibility. We use a three-step milling approach: First Ga-FIB is used to create a rough outline of the antenna, followed by He-FIB to precisely define the antenna shape and finally the gap (see Supplementary Fig. S7). With this combined Ga-/He-FIB approach we are able to realize asymmetric-gap antennas with

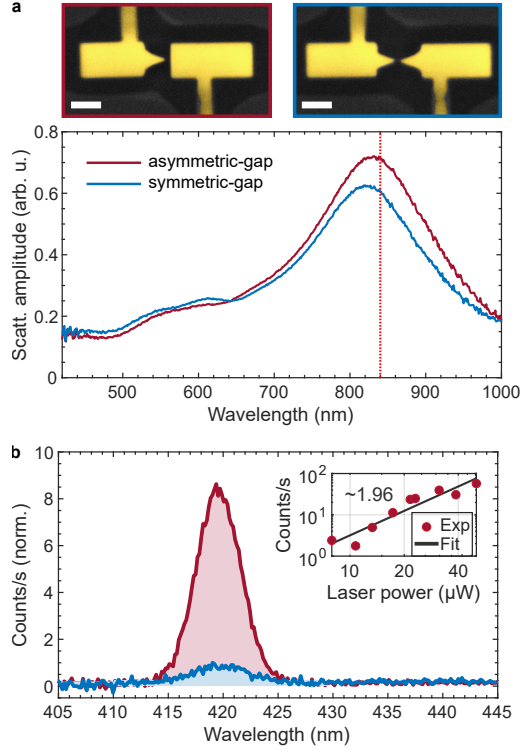


Figure 2: **Influence of the local gap geometry on the SH radiation.** **a**, Top panel: Colored SEM images of an asymmetric-gap and symmetric-gap antenna, respectively. Both antennas have a gap size of 9 nm and tip opening angles of  $40^\circ$ . Scale bars, 50 nm. Bottom panel: Linear white-light scattering spectra. Antennas were designed such that their resonances match the excitation wavelength of 840 nm. A small shoulder at around 550 nm appears for both antennas, which is attributed to the electrical connection wires. For the symmetric-gap antenna, a second peak at 600 nm corresponding to the antibonding mode appears. **b**, SH radiation spectra. Integration time was set to 60 s. The inset shows a bi-logarithmic plot of the power dependence of an exemplary asymmetric-gap antenna confirming the quadratic dependence of the SH signal on the pump power.

ultra-sharp tips exhibiting a radius of curvature at the apex down to 3 nm for a gap size of 8 nm (see Supplementary Section 2.4).

To demonstrate the influence of local symmetry breaking on SHG, we first analyze the SH radiation for two exemplary asymmetric-gap and symmetric-gap antennas with a tip opening angle of  $40^\circ$ . Antennas were fabricated from the same 40 nm-thick gold platelet on a glass substrate and exhibit equal dimensions in the gap region, confirmed by scanning electron microscopy (SEM, top panel of Fig. 2a). Electrical connection wires (vertical structures in Fig. 2a) were included in the design to reduce charging effects during FIB milling and SEM characterization, while hardly affecting the optical response of the antenna.<sup>42</sup> Linear scattering spectra (bottom panel in Fig. 2a) show that both antennas are resonant at 840 nm, which matches the excitation wavelength of the pump laser.

For SH experiments, a pulsed 100 fs titanium-sapphire laser centered at 840 nm is focused with an oil-immersion microscope objective (NA 1.45) through the glass substrate onto individual antennas with the polarization parallel to the long axis of the antenna. Broadening of the laser pulse due to dispersion is precompensated by a prism pulse compressor before the objective (see Supplementary Section 2.2). SH radiation is collected by the same objective and analyzed with a spectrometer after filtering out the pump light.

The recorded spectra in Fig. 2b show that SH radiation from the asymmetric-gap antenna dominates over its symmetric counterpart and exhibits a nearly ten-fold enhancement of radiated SH power, clearly demonstrating the substantial impact of local symmetry breaking on SHG. There remains a small amount of SH yield from the symmetric-gap antenna, which is not expected from the symmetric field enhancement in the gap and therefore vanishing DOA. As we show below, such residual SHG can be attributed to the presence of the so far neglected glass substrate, causing SH radiation due to symmetry breaking along the direction normal to the substrate.

## Quantitative modeling of second harmonic generation

In order to obtain a profound understanding of the SHG process and to validate the calculated values of the field enhancement and DOA presented in Fig. 1, we implemented nonlinear simulations based on a finite element method,<sup>28</sup> that quantitatively describe the SH yield (for more details see Methods and Supplementary Section 1.3). One major challenge in the modeling process is the specific choice of  $\chi_{S,\perp,\perp,\perp}^{(2)}$ , which determines the strength of the SH polarization, see Eq. (2). Various values can be found in literature, either based on theoretical calculations<sup>43–47</sup> or experimental data.<sup>32,33,48–50</sup> For instance, Wang *et al.*<sup>32</sup> used two-beam SHG on a sputtered gold film to retrieve the bulk and surface components of  $\bar{\chi}_S^{(2)}$  for a gold-air interface. These values are commonly applied to model nanoscale systems,<sup>51–53</sup> which typically results in a sufficient qualitative description of SHG. However, we find that none of the above-mentioned values lead to a satisfactory fit to our data (see Supplementary Section 1.4). Moreover, since all antennas are fabricated on a glass substrate, we have to take into account two distinct complex values of the SH susceptibility,  $\chi_a^{(2)}$  for the gold-air and  $\chi_g^{(2)}$  for the gold-glass interface. To overcome the ambiguity in the choice of the SH susceptibilities, we recorded SH radiation patterns (see Fig. 3a) carrying information about the dipole distribution and orientation as well as amplitude and phase of the SH sources, which in turn strongly depends on the relative strengths of  $\chi_a^{(2)}$  and  $\chi_g^{(2)}$  (for a detailed discussion see Supplementary Section 1.4).

We model our data by introducing a complex scaling parameter  $s = |s|e^{i\phi_s}$ , where  $\chi_g^{(2)} = s \cdot \chi_a^{(2)}$ , while  $\chi_a^{(2)}$  is set to 1 (see Fig. 3b). In the first step we calculate radiation patterns for a limited region in the complex plane with amplitude  $|s|$  being scaled between 0 and 2 and phase  $\phi_s$  between 0 and  $2\pi$ . In the following, we demonstrate the strong influence of  $\phi_s$  on the symmetry of the radiation pattern, while we fix  $|s|$  for all simulations shown in Fig. 3 to 0.55 – we show later that this exemplary value is an optimal choice. We focus on simulated radiation patterns polarized along the short axis of an asymmetric-gap antenna (*i.e.* along the  $y$ -direction in Fig. 3a). Depending on  $\phi_s$ , radiation patterns differ immensely

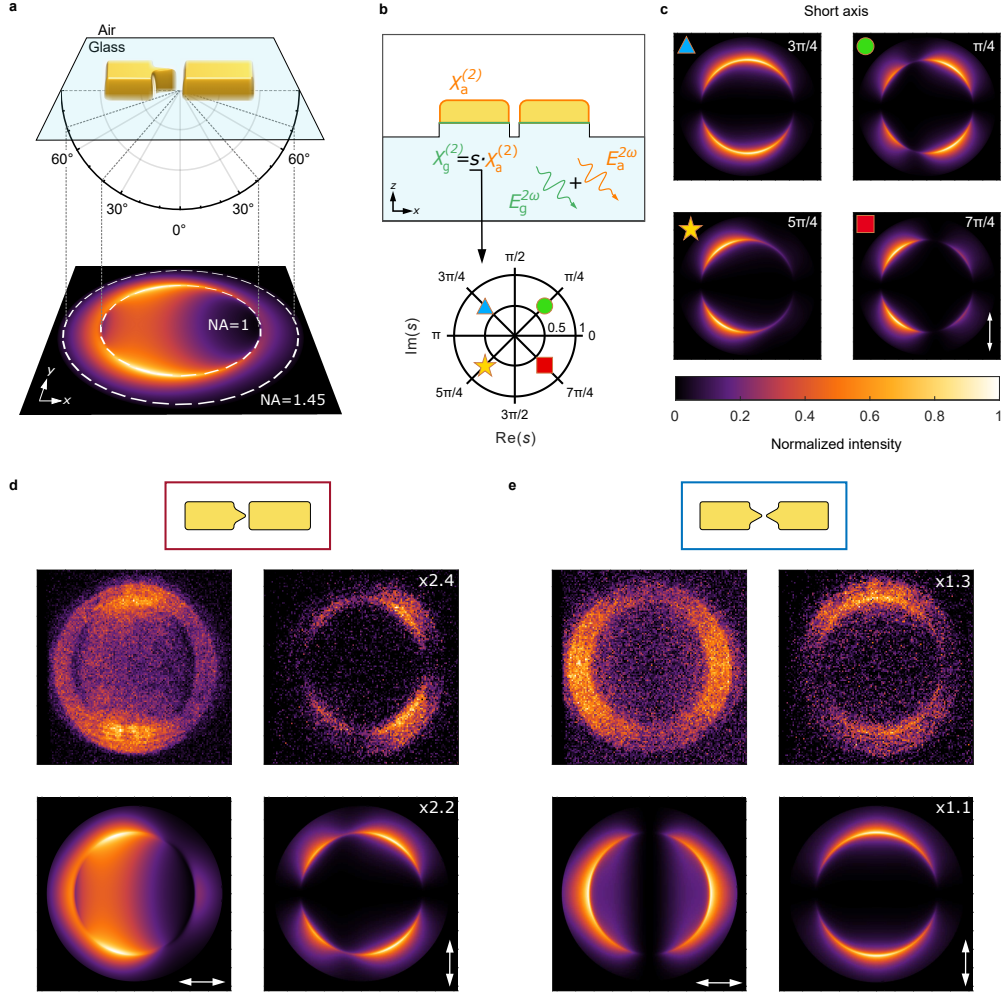


Figure 3: **Simulated and experimental SH radiation patterns.** **a**, Sketch of the emergence of a simulated radiation pattern by projecting the angular radiation pattern onto a plane in the substrate half-space. The critical angle of the glass-air interface and maximum collection angle for a numerical aperture of 1.45 are indicated with white dashed lines. **b**, Schematic  $xz$ -cut through the two antenna rods labeling the two distinct interfaces with corresponding second order susceptibility components, namely gold-air,  $\chi_a^{(2)}$ , and gold-glass,  $\chi_g^{(2)}$ . Lower panel in **b**: Complex plane representation of  $s$ . **c**, Exemplary short axis radiation patterns for an asymmetric-gap antenna. The markers refer to the complex values of  $s$  shown in the lower panel in **b**. **d,e**, Experimental (top) and simulated (bottom) radiation patterns polarized along the long (left panel) and short (right panel) axis for an asymmetric-gap and symmetric-gap antenna, respectively, with  $\alpha = 40^\circ$ . All radiation patterns are normalized to the maximum value of the corresponding long axis pattern. Simulations were performed with  $|s| = 0.55$  and  $\phi_s = 5/18\pi$  rad.

(see Fig. 3c), which makes it possible to determine a coarse range of fitting values of  $\phi_s$  by comparing these simulations to experimentally recorded radiation patterns.

## Experimental radiation patterns

Experimental radiation patterns of an asymmetric-gap and symmetric-gap antenna are obtained by polarization-resolved back focal plane imaging. SH radiation patterns for both long and short axis polarization are displayed in the upper rows of Fig. 3d and e, respectively. The differences in the obtained radiation patterns suggest a distinct character of SH sources: For the symmetric-gap antenna, long and short axis signals are nearly equal and added up they form a rotationally symmetric radiation pattern. Such a radiation pattern is expected for a dipole that is oriented vertically with respect to the substrate, *i.e.* along the  $z$ -direction in Fig. 3b.<sup>54</sup> Thus, for the symmetric-gap antenna, SHG mainly originates from the symmetry breaking due to the substrate. For the asymmetric-gap antenna, symmetry breaking along the long axis of the antenna is dominant. This expectation is indeed reflected in the radiation pattern that resembles that of an  $x$ -oriented SH dipole, being only slightly distorted by a small contribution from the symmetry breaking along  $z$ . In Supplementary Section 1.5 we discuss a semi-analytical approach to calculate these radiation patterns that further supports our model of the SHG process.

Comparison of the experimentally obtained short axis radiation pattern of the asymmetric-gap antenna to the corresponding simulated radiation patterns in Fig. 3c clearly shows that only for the first quadrant value of  $\phi_s$  simulated and experimental radiation patterns match each other. Further analyzing the shape and intensity ratios between long and short axis radiation patterns in more detail results in a limited set of points for  $s$  for which simulation and experiment are consistent (see Supplementary Fig. S5). The lower row in Fig. 3d and e shows a complete series of simulated radiation patterns for  $s = 0.55e^{i5/18\pi}$ . For this particular choice of  $s$ , which is optimal as fully explained later, we achieve excellent agreement between experimental and simulated radiation patterns for both asymmetric-gap and symmetric-gap



antenna indicating that our model accurately describes the SH source.

## Tuning of the SH efficiency

To investigate the dependence of the SH efficiency on the DOA, effectively tuned by the tip opening angle  $\alpha$  as shown in Fig. 1g and h, we performed a series of measurements of asymmetric-gap as well as corresponding symmetric-gap antennas with gradually decreasing  $\alpha$  from  $80^\circ$  down to  $25^\circ$ . Fig. 4 displays the resulting radiated SH power as function of  $\alpha$ , as well as SEM images of antennas with smallest and largest angle. To guarantee comparability down to the involved crystal facets, all antennas were fabricated from the same gold microplatelet (thickness 40 nm) and only antennas with a resonance scattering amplitude  $A_{\text{scatt}}(\lambda_{\text{res}})$  close to the design wavelength of 840 nm, specified by the condition  $A_{\text{scatt}}(840 \text{ nm})/A_{\text{scatt}}(\lambda_{\text{res}}) > 0.9$ , were taken into account (see Supplementary Section 2.3). For each antenna geometry the SH power of at least two nominally identical individual antennas was recorded. The SH power plots show that asymmetric-gap antennas always outperform their symmetric counterparts, especially for small  $\alpha$ , *i.e.* for the strongest local symmetry breaking. Notably, SHG from symmetric-gap antennas also slightly increases for smaller  $\alpha$ .

We apply our numerical model to simulate the tip opening angle dependence of the SH power. The electromagnetic field is strongly concentrated over the antenna tips which is why especially the gap size  $g$  as well as the radius of curvature of the tip  $r$  (see inset in Fig. 4) have a major influence. In experiments it is inevitable that  $r$  decreases for smaller angles and it is therefore reasonable to adjust it also for the simulated geometries based on SEM analysis, while  $g$  is kept constant at average values of 8.1 nm and 9.3 nm for asymmetric-gap and symmetric-gap antennas, respectively (see Supplementary Section 2.4 for a detailed analysis of the geometry parameters). We have seen that the shape of simulated radiation patterns strongly depends on the phase  $\phi_s$ . The information about the tip angle dependence of the SH power contained in Fig. 4 allows us to further confine the range of both,  $\phi_s$  and

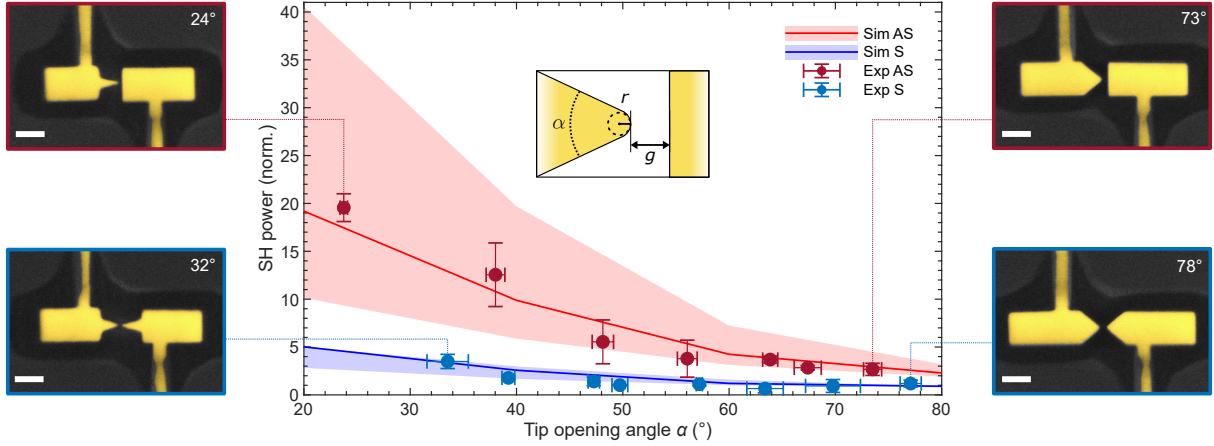


Figure 4: **Tuning SHG by varying the degree of local symmetry breaking.** Measured and simulated SH power from asymmetric-gap (red) and symmetric-gap (blue) antennas as a function of the tip opening angle  $\alpha$ , *i.e.* the degree of local asymmetry. Error bars in the experimental data account for measurements recorded for different nominally equal antennas with comparable linear optical properties. SEM images show antennas with smallest (left panel) and largest (right panel)  $\alpha$  (scale bars, 50 nm). The inset defines additional gap parameters besides  $\alpha$ , namely gap size  $g$  and radius of curvature of the tip  $r$ . Solid lines represent simulations with fixed gap size ( $g = 8.1$  nm and  $g = 9.3$  nm for asymmetric-gap and symmetric-gap antennas, respectively) and adjusted  $r$  according to SEM analysis (see main text). The shaded regions illustrate simulations with  $\Delta g, \Delta r = \pm 1$  nm. Experimental and simulated data are separately normalized to the respective SH power of the symmetric-gap antenna with largest  $\alpha$ .

$|s|$ . To this end, we simulated the tip angle dependent SH power with  $s$  ranging within the predetermined set of possible values based on the previous analysis of radiation patterns. Employing a fitting procedure, discussed in detail in Supplementary Section 1.4, we obtain an optimal value of  $s = 0.55e^{i5/18\pi}$ . Both simulated radiation patterns (Fig. 3d and e) as well as tip angle dependent radiated SH power (solid lines in Fig. 4) fit well to our experimental data. Based on this remarkable quantitative agreement we can conclude that the simulated field enhancement values displayed in Fig. 1g and h accurately describe the experimental field distribution in the antenna gaps, and that the derived quantitative values for the DOA correctly reflect the asymmetry in the field hotspots.

To assess the influence of small-scale changes in the gap geometry on the SH efficiency, we further vary the geometry parameters  $g$  and  $r$  with  $\Delta g, \Delta r = \pm 1$  nm, an uncertainty that follows from the inspection of SEM images. Maximum and minimum values of the shaded regions in Fig. 4 correspond to simulations, where  $g$  and  $r$  are equally modified, *i.e.*  $\Delta g, \Delta r = -1$  nm for maximum and  $\Delta g, \Delta r = +1$  nm for minimum SH power, respectively. For symmetric-gap antennas, varying these parameters does not impact the SH power too much, as the symmetry in the gap is not lifted. Asymmetric-gap antennas, on the contrary, are extremely sensitive to changes in the gap region with more than a 100% boost in SH power for the smallest tip opening angle of  $20^\circ$ . This is also reflected in experiments, where we observe a larger variation of SH power for nominally equal asymmetric-gap antennas, especially towards smaller  $\alpha$ . Nevertheless, nearly all of the investigated antennas lie within the range of  $\Delta g, \Delta r = \pm 1$  nm, which demonstrates the outstanding control and precision we are able to achieve with the presented combined Ga-/He-FIB approach.

## Conclusion

We have realized efficient SHG from plasmonic dimer antenna hotspots by controlling both enhancement and asymmetry of local fields in sub-10 nm gaps. Such local symmetry breaking preserves the large field enhancement of the resonant mode at the FF and circumvents the

silencing effect. The maximal observed nonlinear coefficient ( $\gamma_{\text{SH}} = 1.7 \times 10^{-10} \text{ W}^{-1}$ , see Supplementary Section 2.5) is comparable to the coefficient observed in systems with two resonances ( $\gamma_{\text{SH}} = 5.1 \times 10^{-10} \text{ W}^{-1}$ ), where symmetry is broken globally.<sup>28</sup> By employing He-FIB milling of mono-crystalline gold microplatelets we achieve such high precision and reproducibility that we are able to systematically vary the antenna gap geometry. It is therefore possible to gradually tune the SH radiation by adjusting the opening angle of the sharp tip at the antenna gap.

Recorded SH radiation patterns reveal the orientation and phase relation of SH dipoles determined by the relative strengths of the second-order surface susceptibilities of gold-air and gold-glass interfaces. Full-wave nonlinear simulations result in a simultaneous quantitative matching between simulated and experimentally observed radiation patterns as well as tip angle dependent SH power for both asymmetric-gap and symmetric-gap antennas.

Based on the quantitative analysis we conclude that we reach a field enhancement of up to 175 and a DOA of up to 0.36 in our experiments. Although in similar systems comparable asymmetries can be obtained, field enhancements are an order of magnitude lower.<sup>9-11</sup> We therefore anticipate that our concept of local symmetry breaking opens new possibilities for the realization of efficient nonlinear nanoscale systems, which demand strong field enhancement combined with large local field asymmetry.

## Methods

### Sample fabrication

Mono-crystalline gold microplatelets with a thickness of 40 nm are grown based on a wet-chemical synthesis described in Ref.<sup>55</sup> and are afterwards transferred onto a glass slide with evaporated metal layers featuring an array of circular openings produced by electron beam lithography (20 nm chromium adhesion layer, 80 nm gold layer), see Ref.<sup>56</sup>. The microplatelets are placed on top of sufficiently small holes to ensure conductive connection of flake and metal film. Plasmonic nanoantennas are fabricated using a three-step Ga-/He-FIB

(*ZEISS Orion Nanofab*) approach described in Supplementary Section 2.1.

## **Optical characterization**

To record dark-field white light scattering spectra of asymmetric-gap and symmetric-gap plasmonic nanoantennas, the sample is excited with a collimated beam from a stabilized halogen lamp (Thorlabs SLS201L/M) using an oil-immersion microscope objective (PlanApochromat, 100 $\times$ , NA = 1.45, Nikon). The scattered light is collected via the objective and a circular beam block is used to block direct reflection from the sample. The scattered light is then analyzed by a spectrometer (Shamrock 303i, 80 lines/mm, blazing at 870 nm) equipped with an electron-multiplied charge-coupled device (EMCCD, iXon A-DU897-DC-BVF, Andor).

For SHG measurements a femtosecond pulsed Ti:Sa laser (Mira Optima 900-F, repetition rate 80 MHz, pulse width at laser output 100 fs) is focused through the glass substrate on single antennas, using the same objective and spectrometer as above. Details of the setup and the implemented pulse compression system can be found in the Supplementary Section 2.2. The SH spectra displayed in Fig. 2 have been recorded using a 300 lines/mm grating blazed at 420 nm with an integration time of 60 s, while for recording of the SH radiation in Fig. 4 we used an 80 lines/mm grating blazed at 565 nm and an integration time of 30 s. All spectra are corrected with the total transfer function of the detection path (see Supplementary Section 2.5). To record SH radiation patterns we insert a 1000-mm Bertrand lens before the spectrometer and replace the spectrometer grating by a mirror. Integration times were set to 120 s for asymmetric-gap and 150 s for symmetric-gap antennas, respectively.

## **Numerical simulations**

We perform frequency-domain finite-element simulations to calculate the linear and nonlinear response of the system by using the commercial software package COMSOL Multiphysics. The source employed at the SH (Eq. (2)) is calculated from linear simulations where the

structure is excited from the substrate with a plane wave polarized along the long axis of the antenna. The mesh is generated to match the symmetry of the simulated structure, with a minimum element size of 0.5 nm. SH radiation patterns and SH power values are obtained from far-field calculations using the Matlab toolbox RETOP 8.1,<sup>57</sup> with the near-field collected at the surface of a box 100 nm from the structure. More details about the numerical simulations can be found in the Supplementary Section 1.

## Acknowledgement

We gratefully acknowledge funding by the Deutsche Forschungsgemeinschaft (DFG, German Research Foundation) under Germany's Excellence Strategy through the Würzburg-Dresden Cluster of Excellence on Complexity and Topology in Quantum Matter ct.qmat (EXC 2147, Project ID ST0462019) as well as through a DFG project (INST 93/959-1 FUGG), a regular project (HE5618/10-1), and a Reinhard Koselleck project (HE5618/6-1). The Volkswagen foundation is acknowledged for funding via the Experiment! program (95869). Thorsten Feichtner additionally acknowledges financial support from the European Commission through the Marie Skłodowska-Curie Actions (MSCA) individual fellowship project PoSHGOAT (project- id 837928) and participation in CA19140 (FIT4NANO), supported by COST (European Cooperation in Science and Technology).

The authors thank Marco Finazzi, Michele Celebrano and Paolo Biagioni (all Politecnico Milano) as well as Constantino De Angelis (University of Brescia) for helpful discussions. Furthermore, the authors thank Monika Emmerling and Patrick Pertsch (both University of Würzburg) for substrate preparation and microplatelet transfer.

## Supporting Information Available

Details about numerical simulations: geometry setup, linear simulations, overview over different approaches for nonlinear simulations, analysis of the influence of  $\chi^{(2)}$  on radiation pat-

terns, effective dipole model; Experimental information: three-step milling method, scheme of optical setup, summary linear measurements, analysis of antenna geometries with SEM and AFM, evaluation of efficiency

## References

1. Kauranen, M.; Zayats, A. V. Nonlinear plasmonics. *Nature Photonics* **2012**, *6*, 737–748.
2. Dombi, P.; Pápa, Z.; Vogelsang, J.; Yalunin, S. V.; Sivilis, M.; Herink, G.; Schäfer, S.; Groß, P.; Ropers, C.; Lienau, C. Strong-field nano-optics. *Reviews of Modern Physics* **2020**, *92*, 025003.
3. Bonacina, L.; Brevet, P.-F.; Finazzi, M.; Celebrano, M. Harmonic generation at the nanoscale. *Journal of Applied Physics* **2020**, *127*, 230901.
4. Rybka, T.; Ludwig, M.; Schmalz, M. F.; Knittel, V.; Brida, D.; Leitenstorfer, A. Sub-cycle optical phase control of nanotunnelling in the single-electron regime. *Nature Photonics* **2016**, *10*, 667–670.
5. Ludwig, M.; Aguirregabiria, G.; Ritzkowsky, F.; Rybka, T.; Marinica, D. C.; Aizpurua, J.; Borisov, A. G.; Leitenstorfer, A.; Brida, D. Sub-femtosecond electron transport in a nanoscale gap. *Nature Physics* **2019**, 1–5.
6. Ward, D. R.; Hüser, F.; Pauly, F.; Cuevas, J. C.; Natelson, D. Optical rectification and field enhancement in a plasmonic nanogap. *Nature Nanotechnology* **2010**, *5*, 732–736.
7. Piltan, S.; Sievenpiper, D. Optical rectification using geometrical field enhancement in gold nano-arrays. *Journal of Applied Physics* **2017**, *122*, 183101.
8. Dasgupta, A.; Mennemanteuil, M.-M.; Buret, M.; Cazier, N.; Colas-des Francs, G.; Bouhelier, A. Optical wireless link between a nanoscale antenna and a transducing rectenna. *Nature Communications* **2018**, *9*.

9. Karnetzky, C.; Zimmermann, P.; Trummer, C.; Duque Sierra, C.; Wörle, M.; Kienberger, R.; Holleitner, A. Towards femtosecond on-chip electronics based on plasmonic hot electron nano-emitters. *Nature Communications* **2018**, *9*, 2471.
10. Zimmermann, P.; Hötger, A.; Fernandez, N.; Nolinder, A.; Müller, K.; Finley, J. J.; Holleitner, A. W. Toward Plasmonic Tunnel Gaps for Nanoscale Photoemission Currents by On-Chip Laser Ablation. *Nano Letters* **2019**, *19*, 1172–1178.
11. Shi, L.; Babushkin, I.; Husakou, A.; Melchert, O.; Frank, B.; Yi, J.; Wetzl, G.; Demircan, A.; Lienau, C.; Giessen, H.; Ivanov, M.; Morgner, U.; Kovacev, M. Femtosecond Field-Driven On-Chip Unidirectional Electronic Currents in Nonadiabatic Tunneling Regime. *Laser & Photonics Reviews* **2021**, *15*, 2000475.
12. Heersche, H. B.; Lientschnig, G.; O’Neill, K.; van der Zant, H. S. J.; Zandbergen, H. W. *In situ* imaging of electromigration-induced nanogap formation by transmission electron microscopy. *Applied Physics Letters* **2007**, *91*, 072107.
13. Stolz, A.; Berthelot, J.; Mennemanteuil, M.-M.; Colas des Francs, G.; Markey, L.; Meunier, V.; Bouhelier, A. Nonlinear Photon-Assisted Tunneling Transport in Optical Gap Antennas. *Nano Letters* **2014**, *14*, 2330–2338.
14. Butet, J.; Brevet, P.-F.; Martin, O. J. F. Optical Second Harmonic Generation in Plasmonic Nanostructures: From Fundamental Principles to Advanced Applications. *ACS Nano* **2015**, *9*, 10545–10562.
15. Boyd, R. W. *Nonlinear optics*, 4th ed.; Academic Press is an imprint of Elsevier: San Diego, 2019.
16. Biagioni, P.; Huang, J.-S.; Hecht, B. Nanoantennas for visible and infrared radiation. *Reports on Progress in Physics* **2012**, *75*, 024402.



17. Hasan, S. B.; Lederer, F.; Rockstuhl, C. Nonlinear plasmonic antennas. *Materials Today* **2014**, *17*, 478–485.
18. Finazzi, M.; Biagioni, P.; Celebrano, M.; Duò, L. Selection rules for second-harmonic generation in nanoparticles. *Physical Review B* **2007**, *76*, 125414.
19. Berthelot, J.; Bachelier, G.; Song, M.; Rai, P.; Colas des Francs, G.; Dereux, A.; Bouhelier, A. Silencing and enhancement of second-harmonic generation in optical gap antennas. *Optics Express* **2012**, *20*, 10498.
20. Canfield, B. K.; Husu, H.; Laukkanen, J.; Bai, B.; Kuittinen, M.; Turunen, J.; Kauranen, M. Local Field Asymmetry Drives Second-Harmonic Generation in Noncentrosymmetric Nanodimers. *Nano Letters* **2007**, *7*, 1251–1255.
21. Zhang, Y.; Grady, N. K.; Ayala-Orozco, C.; Halas, N. J. Three-Dimensional Nanostructures as Highly Efficient Generators of Second Harmonic Light. *Nano Letters* **2011**, *11*, 5519–5523.
22. Black, L.-J.; Wiecha, P. R.; Wang, Y.; de Groot, C. H.; Paillard, V.; Girard, C.; Muskens, O. L.; Arbouet, A. Tailoring Second-Harmonic Generation in Single L-Shaped Plasmonic Nanoantennas from the Capacitive to Conductive Coupling Regime. *ACS Photonics* **2015**, *2*, 1592–1601.
23. Czaplicki, R.; Mäkitalo, J.; Siikanen, R.; Husu, H.; Lehtolahti, J.; Kuittinen, M.; Kauranen, M. Second-Harmonic Generation from Metal Nanoparticles: Resonance Enhancement versus Particle Geometry. *Nano Letters* **2015**, *15*, 530–534.
24. Liu, Y., *et al.* Enhancement of second-harmonic generation from Fano plasmonic metasurfaces by introducing structural asymmetries. *Optics Express* **2022**, *30*, 42440–42453.
25. Li, G.-C.; Lei, D.; Qiu, M.; Jin, W.; Lan, S.; Zayats, A. V. Light-induced symme-

- try breaking for enhancing second-harmonic generation from an ultrathin plasmonic nanocavity. *Nature Communications* **2021**, *12*, 4326.
26. Thyagarajan, K.; Rivier, S.; Lovera, A.; Martin, O. J. Enhanced second-harmonic generation from double resonant plasmonic antennae. *Optics Express* **2012**, *20*, 12860.
  27. Aouani, H.; Navarro-Cia, M.; Rahmani, M.; Sidiropoulos, T. P. H.; Hong, M.; Oulton, R. F.; Maier, S. A. Multiresonant Broadband Optical Antennas As Efficient Tunable Nanosources of Second Harmonic Light. *Nano Letters* **2012**, *12*, 4997–5002.
  28. Celebrano, M.; Wu, X.; Baselli, M.; Großmann, S.; Biagioni, P.; Locatelli, A.; De Angelis, C.; Cerullo, G.; Osellame, R.; Hecht, B.; Duò, L.; Ciccacci, F.; Finazzi, M. Mode matching in multiresonant plasmonic nanoantennas for enhanced second harmonic generation. *Nature Nanotechnology* **2015**, *10*, 412–417.
  29. Gennaro, S. D.; Rahmani, M.; Giannini, V.; Aouani, H.; Sidiropoulos, T. P. H.; Navarro-Cía, M.; Maier, S. A.; Oulton, R. F. The Interplay of Symmetry and Scattering Phase in Second Harmonic Generation from Gold Nanoantennas. *Nano Letters* **2016**, *16*.
  30. Liu, S.-D.; Leong, E. S. P.; Li, G.-C.; Hou, Y.; Deng, J.; Teng, J. H.; Ong, H. C.; Lei, D. Y. Polarization-Independent Multiple Fano Resonances in Plasmonic Nonamers for Multimode-Matching Enhanced Multiband Second-Harmonic Generation. *ACS Nano* **2016**, *10*, 1442–1453.
  31. Reddy, K. N.; Chen, P. Y.; Fernández-Domínguez, A. I.; Sivan, Y. Revisiting the boundary conditions for second-harmonic generation at metal-dielectric interfaces. *Journal of the Optical Society of America B* **2017**, *34*, 1824.
  32. Wang, F. X.; Rodríguez, F. J.; Albers, W. M.; Ahorinta, R.; Sipe, J. E.; Kauranen, M. Surface and bulk contributions to the second-order nonlinear optical response of a gold film. *Physical Review B* **2009**, *80*, 233402.

33. Bachelier, G.; Butet, J.; Russier-Antoine, I.; Jonin, C.; Benichou, E.; Brevet, P.-F. Origin of optical second-harmonic generation in spherical gold nanoparticles: Local surface and nonlocal bulk contributions. *Physical Review B* **2010**, *82*, 235403.
34. Chirumamilla, M.; Toma, A.; Gopalakrishnan, A.; Das, G.; Zaccaria, R. P.; Krahne, R.; Rondanina, E.; Leoncini, M.; Liberale, C.; De Angelis, F.; Di Fabrizio, E. 3D Nanostar Dimers with a Sub-10-nm Gap for Single-/Few-Molecule Surface-Enhanced Raman Scattering. *Advanced Materials* **2014**, *26*, 2353–2358.
35. Park, H.; Lim, A. K. L.; Alivisatos, A. P.; Park, J.; McEuen, P. L. Fabrication of metallic electrodes with nanometer separation by electromigration. *Applied Physics Letters* **1999**, *75*, 301–303.
36. Xiang, D.; Jeong, H.; Lee, T.; Mayer, D. Mechanically Controllable Break Junctions for Molecular Electronics. *Advanced Materials* **2013**, *25*, 4845–4867.
37. Laible, F.; Braun, K.; Hauler, O.; Eberle, M.; Kern, D. P.; Meixner, A. J.; Fleischer, M. A flexible platform for controlled optical and electrical effects in tailored plasmonic break junctions. *Nanophotonics* **2020**, *9*, 1391–1400.
38. Baumberg, J. J.; Aizpurua, J.; Mikkelsen, M. H.; Smith, D. R. Extreme nanophotonics from ultrathin metallic gaps. *Nature Materials* **2019**,
39. Lim, D.-K.; Jeon, K.-S.; Kim, H. M.; Nam, J.-M.; Suh, Y. D. Nanogap-engineerable Raman-active nanodumbbells for single-molecule detection. *Nature Materials* **2010**, *9*, 60–67.
40. Huang, J.-S.; Callegari, V.; Geisler, P.; Brüning, C.; Kern, J.; Prangma, J. C.; Wu, X.; Feichtner, T.; Ziegler, J.; Weinmann, P.; Kamp, M.; Forchel, A.; Biagioni, P.; Sennhauser, U.; Hecht, B. Atomically flat single-crystalline gold nanostructures for plasmonic nanocircuitry. *Nature Communications* **2010**, *1*, 150.

41. Kollmann, H.; Piao, X.; Esmann, M.; Becker, S. F.; Hou, D.; Huynh, C.; Kautschor, L.-O.; Bösker, G.; Vieker, H.; Beyer, A.; Götzhäuser, A.; Park, N.; Vogelgesang, R.; Silies, M.; Lienau, C. Toward Plasmonics with Nanometer Precision: Nonlinear Optics of Helium-Ion Milled Gold Nanoantennas. *Nano Letters* **2014**, *14*, 4778–4784.
42. Prangma, J. C.; Kern, J.; Knapp, A. G.; Grossmann, S.; Emmerling, M.; Kamp, M.; Hecht, B. Electrically Connected Resonant Optical Antennas. *Nano Letters* **2012**, *12*, 3915–3919.
43. Rudnick, J.; Stern, E. A. Second-Harmonic Radiation from Metal Surfaces. *Physical Review B* **1971**, *4*, 4274–4290.
44. Sipe, J. E.; So, V. C. Y.; Fukui, M.; Stegeman, G. I. Analysis of second-harmonic generation at metal surfaces. *Physical Review B* **1980**, *21*, 4389–4402.
45. Maystre, D.; Neviere, M.; Reinisch, R. Nonlinear polarisation inside metals: A mathematical study of the free-electron model. *Applied Physics A Solids and Surfaces* **1986**, *39*, 115–121.
46. Benedetti, A.; Centini, M.; Sibilìa, C.; Bertolotti, M. Engineering the second harmonic generation pattern from coupled gold nanowires. *Journal of the Optical Society of America B* **2010**, *27*, 408.
47. Antonietta Vincenti, M.; Campione, S.; de Ceglia, D.; Capolino, F.; Scalora, M. Gain-assisted harmonic generation in near-zero permittivity metamaterials made of plasmonic nanoshells. *New Journal of Physics* **2012**, *14*, 103016.
48. van Nieuwstadt, J. A. H.; Sandtke, M.; Harmsen, R. H.; Segerink, F. B.; Prangma, J. C.; Enoch, S.; Kuipers, L. Strong Modification of the Nonlinear Optical Response of Metallic Subwavelength Hole Arrays. *Physical Review Letters* **2006**, *97*, 146102.

49. Krause, D.; Teplin, C. W.; Rogers, C. T. Optical surface second harmonic measurements of isotropic thin-film metals: Gold, silver, copper, aluminum, and tantalum. *Journal of Applied Physics* **2004**, *96*, 3626–3634.
50. Boroviks, S.; Yezekyan, T.; Rodríguez Echarri, A.; García de Abajo, F. J.; Cox, J. D.; Bozhevolnyi, S. I.; Mortensen, N. A.; Wolff, C. Anisotropic second-harmonic generation from monocrystalline gold flakes. *Optics Letters* **2021**, *46*, 833.
51. Papoff, F.; McArthur, D.; Hourahine, B. Coherent control of radiation patterns of nonlinear multiphoton processes in nanoparticles. *Scientific Reports* **2015**, *5*, 12040.
52. O'Brien, K.; Suchowski, H.; Rho, J.; Salandrino, A.; Kante, B.; Yin, X.; Zhang, X. Predicting nonlinear properties of metamaterials from the linear response. *Nature Materials* **2015**, *14*, 379–383.
53. Deng, J.; Tang, Y.; Chen, S.; Li, K.; Zayats, A. V.; Li, G. Giant Enhancement of Second-Order Nonlinearity of Epsilon-near-Zero Medium by a Plasmonic Metasurface. *Nano Letters* **2020**, *20*, 5421–5427.
54. Bouhelier, A.; Beversluis, M.; Hartschuh, A.; Novotny, L. Near-Field Second-Harmonic Generation Induced by Local Field Enhancement. *Physical Review Letters* **2003**, *90*, 013903.
55. Krauss, E.; Kullock, R.; Wu, X.; Geisler, P.; Lundt, N.; Kamp, M.; Hecht, B. Controlled Growth of High-Aspect-Ratio Single-Crystalline Gold Platelets. *Crystal Growth & Design* **2018**, *18*, 1297–1302.
56. Kern, J.; Kullock, R.; Prangma, J.; Emmerling, M.; Kamp, M.; Hecht, B. Electrically driven optical antennas. *Nature Photonics* **2015**, *9*, 582–586.
57. Yang, J.; Hugonin, J.-P.; Lalanne, P. Near-to-far field transformations for radiative and guided waves. *ACS photonics* **2016**, *3*, 395–402.

# Supplementary material

## Controlling field asymmetry in nanoscale gaps for second harmonic generation

Jessica Meier<sup>1</sup>, Luka Zurak<sup>1</sup>, Andrea Locatelli<sup>2</sup>, Thorsten Feichtner<sup>1</sup>, René Kullock<sup>1</sup>, and Bert Hecht<sup>1</sup>

<sup>1</sup>Nano-Optics and Biophotonics Group, Experimental Physics 5, Institute of Physics, University of Würzburg, Germany

<sup>2</sup>Department of Information Engineering, University of Brescia, Italy

### Contents

<b>1</b>	<b>Numerical simulations</b>	<b>2</b>
1.1	Overview . . . . .	2
1.2	Linear simulations . . . . .	3
1.3	Nonlinear simulations . . . . .	3
1.4	Influence of $\chi^{(2)}$ on radiation patterns . . . . .	5
1.5	Semi-analytical calculation of radiation patterns - effective dipole model . . . . .	7
<b>2</b>	<b>Experiments</b>	<b>10</b>
2.1	Fabrication . . . . .	10
2.2	Optical setup for SHG measurements . . . . .	10
2.3	Linear properties . . . . .	11
2.4	Antenna geometry . . . . .	11
2.5	Evaluation of efficiency . . . . .	13

arXiv:2210.14105v5 [physics.optics] 2 Mar 2023

# 1 Numerical simulations

## 1.1 Overview

The FEM simulations discussed in the main text were performed using COMSOL Multiphysics® 6.0 [1]. We used the “Wave Optics Module” to solve Maxwell’s equations in the frequency domain for our system in a two step process. First, we analyze the linear response of the system, which is then used to calculate  $\mathbf{P}_S^{(2\omega)}$  according to Eq. (2) in the main text. In the second step, we use this source to drive the system at SH.

The first task is to find the geometry which exhibits a bonding mode resonance at 840 nm, the wavelength of the pump laser. For all scenarios under consideration, the antenna is placed on top of a glass substrate (see Fig. S1a). The simulation region, as in the exemplary case, is a sphere with radius of 600 nm, where the volume surrounding the antenna has a radius  $r_{\text{sur}} = 400$  nm. In addition, a perfectly matched layer (PML) with thickness  $t_{\text{PML}} = 200$  nm is introduced to mimic an open and non-reflecting infinite domain.

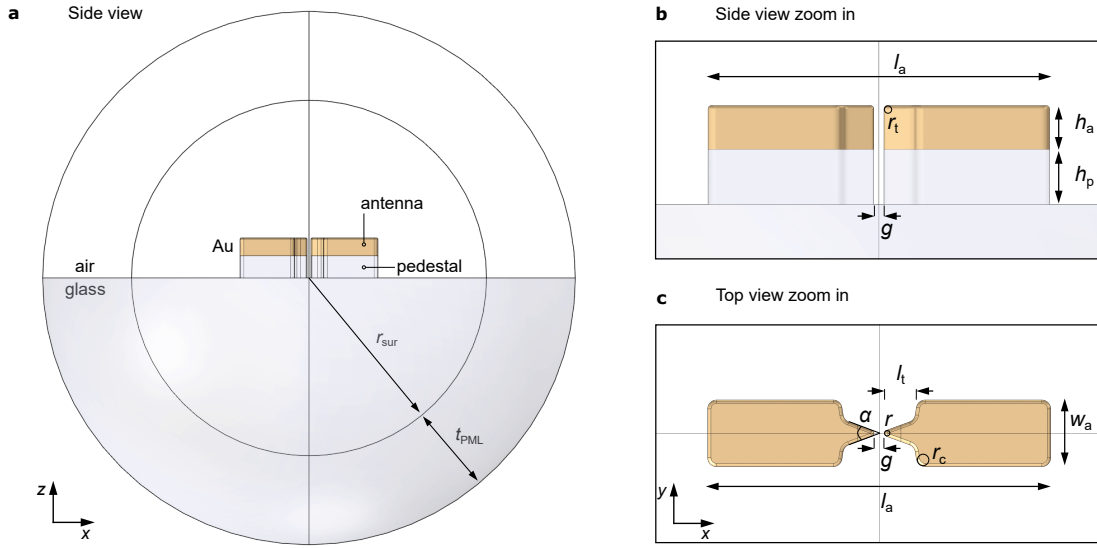


FIG. S1: **Geometry used for COMSOL simulations.** **a**, Side view of the complete simulation volume. The gold antenna is situated on top of a glass pedestal above a glass substrate. **b**, Side view zoom to the antenna area.  $l_a$  is the length of the antenna,  $h_a$  is the antenna height,  $h_p$  is the height of the glass pedestal,  $r_t$  is the radius of curvature of the antenna at the tip. **c**, Top view of the antenna area.  $l_t$  is the tip length,  $\alpha$  is the tip opening angle,  $r$  is the radius of curvature at the tip,  $g$  is the gap size,  $w_a$  is the width of the antenna, and  $r_c$  is the radius of curvature of the antenna corners.

Heights of the gold antenna and the pedestal on which it resides due to He-FIB milling into the substrate, as sketched in the side view in Fig. S1b, are obtained from atomic force microscopy (AFM) measurements. The height of the gold platelet used as starting material is retrieved by optical transmission measurements (as discussed in [2]). In a typical structure, the antenna height  $h_a$  is 40 nm, while the pedestal, produced during He-FIB milling, has a height of 50 nm. Moreover, the lateral dimensions as shown in the top view in Fig. S1c, are extracted from SEM images. AFM and SEM analysis are discussed in more detail in section 2.4. In all cases, antennas have been designed to have a width  $w_a$  of 60 nm and a tip length  $l_t$  of 30 nm, while the radius of curvature of the antenna corners  $r_c$  is kept constant at 8 nm and radius of curvature at the tip  $r_t$  at 3 nm. The tip opening angle  $\alpha$  has been varied from  $20^\circ$  to  $80^\circ$ . The radius of curvature of the tip  $r$  has been adapted for each structure, where smaller angles lead to sharper tips. Moreover, changes of the tip opening angle lead to changes in the coupling strength between two antenna arms. Therefore, the length of the antenna rods has been adapted for each tip opening angle to re-adjust the bonding mode resonance to 840 nm.

## 1.2 Linear simulations

The linear response of the system, that is the scattering spectrum and the near-field response, are simulated using the scattered field formulation implemented in COMSOL. Since the size of the collimated beam that is used for excitation in the white-light scattering experiment is approximately  $2\ \mu\text{m}$ , we use a plane wave propagating in  $+z$  direction, polarized along the long axis of the antenna as excitation source (background field). Due to the presence of the glass-air interface the background field is calculated from s-polarized Fresnel coefficients for the glass and the air half-space separately. The excitation wavelength ranges from 400 to 1000 nm and is discretized in steps of 10 nm. The refractive index of glass is modeled using Sellmeier coefficients for borosilicate crown glass [3], while the permittivity of gold is modeled using single-crystal experimental data by Olmon et al. [4], as it has been demonstrated to accurately represent the optical response of our gold microplatelets (see [2]).

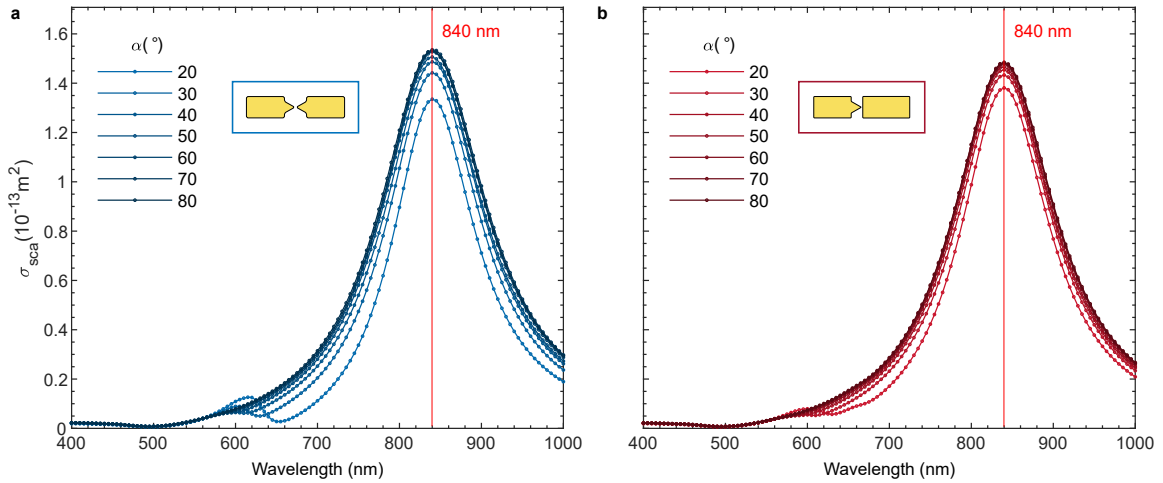


FIG. S2: **Linear spectra.** Scattering cross sections of asymmetric-gap **a**, and symmetric-gap **b**, antennas for different tip opening angles from  $20^\circ$  to  $80^\circ$ . All geometries were optimized such that the peak of the fundamental bonding mode resonance is at 840 nm.

Scattering cross sections are presented in Fig. S2a,b for symmetric-gap and asymmetric-gap antennas, respectively. The geometry of each antenna is optimized to bring the bonding mode resonance to 840 nm by changing  $l_a$ . The small peak at 600 nm corresponds to the antibonding resonance as verified by inspection of its mode pattern. All of the structures show only weak response at 420 nm, corresponding to the SH wavelength, providing us with the possibility to test how symmetry breaking influences SHG without major influence by antenna-enhanced radiation effects.

Using Eq. (4) from the main text we can calculate the expectation for the SH signal considering only the field at FF. From such simple considerations it is expected to observe no SHG from symmetric-gap antennas, while in the case of asymmetric-gap antennas SHG can be tuned by a factor of 30 by changing the tip opening angle from  $80^\circ$  to  $20^\circ$  (see Fig. S3).

## 1.3 Nonlinear simulations

As discussed in the main text, the second order nonlinearity of gold nanoantennas originates from breaking the centrosymmetry of the gold crystal lattice at the surface of the structure, with  $\chi_{S,\perp,\perp,\perp}^{(2)}$  being the dominant term of the  $\bar{\chi}_S^{(2)}$  tensor. Other nonlinear components, such as  $\chi_{S,\parallel,\perp,\perp}^{(2)}$  as well as bulk contribution (values taken from Ref. [5]), have been tested and show no significant influence on the SH response of our system. Due to the discontinuity of the electric field normal component at the surface, a controversy existed regarding whether the inside or the outside field at FF should be taken to evaluate the SH response, which was resolved by Sipe et al. [6]. They have demonstrated that in order to accurately model SH from metal surfaces, the FF fields from inside the metal should be utilized and generated SH sources should be placed just outside of the metal.



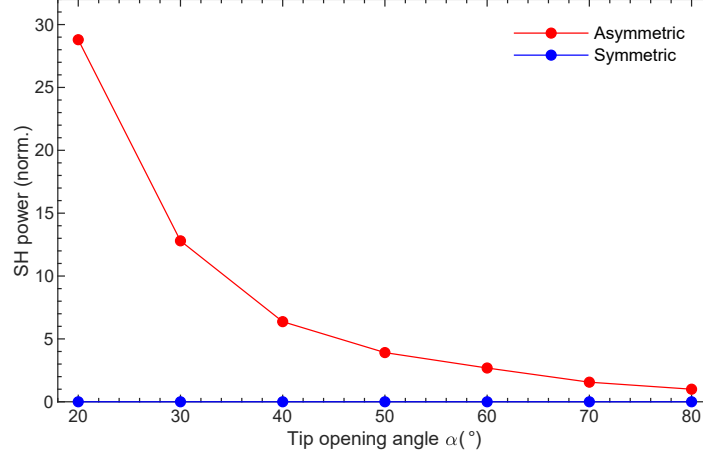


FIG. S3: **SHG expectation from linear simulations.** Radiated SH power depending on the tip opening angle as expected from linear simulations.

There are several approaches to include surface sources into Maxwell's equations, and subsequently to couple them to a numerical solver. One of the possibilities has been explored by Reddy et al. [7], who introduced polarization sources at the interface via modified boundary conditions. The new boundary condition for the tangential component of the electric field  $\mathbf{E}_{\parallel}$ , in the presence of the current oscillating perpendicular to the surface, reads as

$$\Delta \mathbf{E}_{\parallel}^{(2\omega)} = -\frac{1}{\epsilon'} \nabla_{\parallel} P_{S,\perp}^{(2\omega)}(\mathbf{r}_S), \quad (1)$$

where  $\nabla_{\parallel}$  is the tangential component of the vector derivative,  $P_{S,\perp}^{(2\omega)}$  is the perpendicular component of the SH polarization source and  $\epsilon'$  is the permittivity of the surrounding medium at SH. One of the limitations of this method becomes obvious when considering structures which do not have a smooth surface (as in our case), yielding an undefined vector derivative  $\nabla_{\parallel}$ . We have also considered the auxiliary field method introduced by Yang et al. within their framework for general electromagnetism at the nanoscale [8]. With this approach, it is possible to circumvent the need for calculating vector derivatives tangential to the surface, rendering the method more robust. However, by introducing auxiliary fields, simulation time is prolonged as it requires the use of more stable non-iterative solvers. Finally, we have implemented SH sources directly by stating them in the weak form as it was shown by Yang and Ciraci [9]. We present a simple derivation of the weak form starting from Maxwell's wave equation for the electric field

$$\nabla \times \frac{1}{\mu} \nabla \times \mathbf{E} - \frac{\omega^2}{c^2} \epsilon \mathbf{E} = -i\omega \mu_0 \mathbf{j}. \quad (2)$$

Here we adopt the engineering  $+i\omega t$  convention as it is used in COMSOL, yielding a negative sign for the current term. If we consider an arbitrary current source oscillating perpendicular to the surface  $\mathbf{j} = j_S \hat{\mathbf{r}}_{\perp} \delta(\mathbf{r} - \mathbf{r}_S)$ , where  $j_S$  can be expressed via polarization  $P_S$ , i.e.  $j_S = \partial_t P_S$ , then by multiplying this expression with the test field  $\tilde{\mathbf{E}}$  and integrating over the whole volume we obtain

$$\int_V dV \left[ \nabla \times \frac{1}{\mu} \nabla \times \mathbf{E} - \frac{\omega^2}{c^2} \epsilon \mathbf{E} \right] \cdot \tilde{\mathbf{E}} = \omega^2 \mu_0 \int_V dV P_S \cdot \tilde{\mathbf{E}}. \quad (3)$$

The volume integral on the right side collapses to a surface integral yielding a surface contribution in the weak form

$$\omega^2 \mu_0 \int_S dS P_{S,\perp} \tilde{\mathbf{E}}_{\perp}. \quad (4)$$

To put the methods to test, we have inspected the influence of the shape of the sharp edges on the SH radiation patterns. The results provided by the weak form are independent of small changes in the geometry of the structure close to sharp edges which is not the case for the boundary condition method. Therefore, from the considered methods the weak form method provides the most robust and economical way to simulate SH response.

#### 1.4 Influence of $\chi^{(2)}$ on radiation patterns

One of the main uncertainties when it comes to modeling the nonlinear response of antennas, is the uncertainty in the experimentally obtained numerical values of  $\chi_{S_i, \pm, \pm, \pm}^{(2)}$  (shorthand notation  $\chi^{(2)}$ ) for different interfaces. In this section we therefore analyze the influence of  $\chi^{(2)}$  on radiation pattern and radiated power of the system under investigation.

As a starting point we perform nonlinear simulations by choosing the experimentally obtained  $\chi_a^{(2)} = 6.5 \cdot 10^{-18} \text{m}^2/\text{V}$  value measured by Wang et al. [5], which has been determined for a gold-air interface. It is common practice to use the same value of the parameter on the other interfaces as well [10], in our case the gold-glass interface. Using this simplification we calculate radiation patterns of our antenna structures using the far-field expansion Matlab toolbox RETOP 8.1 [11]. The second row of Fig. S4 shows that the radiation patterns for the short axis of the asymmetric-gap antenna and both radiation patterns of the symmetric-gap antenna do not fit to the corresponding experimental data displayed in the first row of the figure. To resolve this evident discrepancy we have tested theoretically calculated  $\chi^{(2)}$  parameters which depend on the dielectric material neighboring the gold interface [12, 13]. Implementing the formula for  $\chi^{(2)}$  given in this publication yields for the gold-air interface  $\chi_a^{(2)} = (3.8 - i0.5) \cdot 10^{-18} \text{m}^2/\text{V}$  and  $\chi_g^{(2)} = (-0.8 + i0.1) \cdot 10^{-18} \text{m}^2/\text{V}$  for the gold-glass interface, respectively. However, this choice of  $\chi^{(2)}$  values does not yield a better match between simulations and experiment as it can be seen by inspecting the bottom row in Fig. S4.

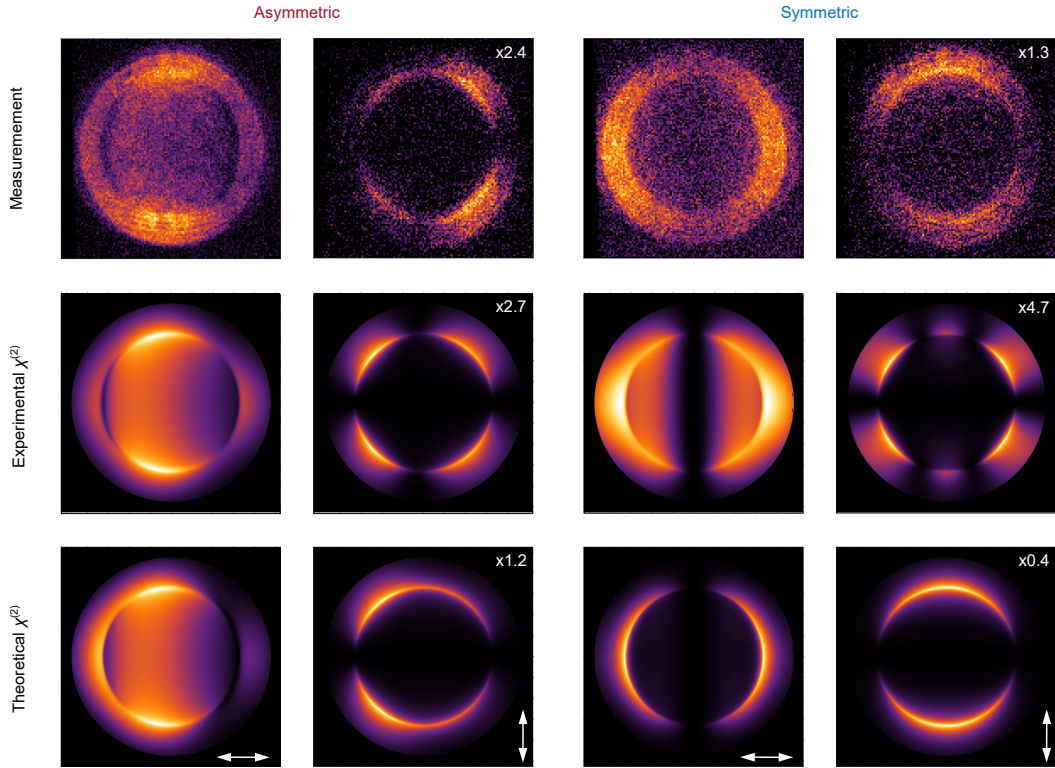


FIG. S4: **Radiation patterns for  $\chi^{(2)}$  values taken from the literature.** For comparison, the first row displays the measured radiation patterns also shown in Fig. 3 in the main text. In the second row radiation patterns are plotted using the experimentally determined value of  $\chi^{(2)}$  according to Ref. [5]. In the third row,  $\chi^{(2)}$  values for two interfaces have been calculated using a formula derived in Refs. [12, 13].

Due to this uncertainty it seems to be appropriate to use  $\chi^{(2)}$  as a fitting parameter. Note that the general formula for the response of the system upon driving it with the source  $\mathbf{P}_S$  is linear. According to [14] the electric field at any position  $\mathbf{r}$  can be calculated from the following expression

$$\mathbf{E}(\mathbf{r}) = \frac{\omega^2 \mu}{\epsilon_0 c^2} \int_{V_0} \overleftrightarrow{\mathbf{G}}_{tot}(\mathbf{r}, \mathbf{r}_0) \mathbf{P}_S(\mathbf{r}_0) d\mathbf{r}_0^3. \quad (5)$$

Here,  $\mu$  is the relative permeability of the surrounding medium and  $\overleftrightarrow{\mathbf{G}}_{tot}(\mathbf{r}, \mathbf{r}_0)$  is a dyadic Green's function, representing the response of the system at position  $\mathbf{r}$  upon point source excitation at position  $\mathbf{r}_0$ . The integration is performed over the antenna volume  $V_0$ . In the case of a homogeneous interface, a change in  $\chi^{(2)}$  does not affect the resulting radiation pattern  $p(\mathbf{r}) \propto |\mathbf{E}(\mathbf{r})|^2$ , and only influences the total radiated power  $P_{SH} = \int p(\mathbf{r}) d\Omega$ . However, since our system has two interfaces with different non-negligible SH source contributions – gold-glass and gold-air interface – we have to split the integral and consider a correct scaling of both  $\chi^{(2)}$  parameters. Therefore, we state Eq. (5) in the following form

$$\mathbf{E}(\mathbf{r}) = s_a \mathbf{E}_{a0}(\mathbf{r}) + s_g \mathbf{E}_{g0}(\mathbf{r}), \quad (6)$$

where  $s_a$  and  $s_g$  are scaling factors for the respective  $\chi^{(2)}$  parameters, such that  $\chi_a^{(2)} = s_a \chi_{a0}^{(2)}$ ,  $\chi_g^{(2)} = s_g \chi_{g0}^{(2)}$ .  $\mathbf{E}_{a0}(\mathbf{r})$  and  $\mathbf{E}_{g0}(\mathbf{r})$  are fields radiated by the antenna, driven only by sources at the respective interfaces, where in both cases we apply the normalization  $\chi^{(2)} = 1 \text{ m}^2/\text{V}$ . Taking the absolute square of the total field yields

$$|\mathbf{E}(\mathbf{r})|^2 = |s_a|^2 \left\{ |\mathbf{E}_{a0}(\mathbf{r})|^2 + \left| \frac{s_g}{s_a} \right|^2 |\mathbf{E}_{g0}(\mathbf{r})|^2 + 2 \left| \frac{s_g}{s_a} \right| |\mathbf{E}_{g0}(\mathbf{r})| |\mathbf{E}_{a0}(\mathbf{r})| \cos(\Delta\phi_0 + \Delta\phi_s) \right\}, \quad (7)$$

where  $\Delta\phi_0 = \phi_{g0} - \phi_{a0}$  is the phase difference for the case of  $s_a = s_g = 1$ , while  $\Delta\phi_s = \phi_g - \phi_a$  is the phase difference due to scaling. We can see that the shape of the radiation pattern depends on the relative size of the  $\chi^{(2)}$  parameters – since they are complex-valued numbers, radiation patterns depend on the relative magnitudes and phase differences of the two nonlinear susceptibilities. Therefore, we keep one of the two parameters constant and scale the other. We choose to fix  $s_a = 1$  and scale  $s_g$  (from here on referred to as  $s$ ) in the complex plane, that is we scale the gold-glass susceptibility relative to the gold-air susceptibility  $\chi_g^{(2)} = s \cdot \chi_a^{(2)}$ .

To match the experimental data with simulations, we considered both types of experimental results presented in the main text: radiation patterns for a fixed angle ( $40^\circ$  – see Fig. 3 in the main text) and SH power depending on the tip opening angle (Fig. 4 in the main text). In a first step we calculate radiation patterns for a limited region in the complex plane for amplitudes  $|s|$  between 0 and 2 in steps of 0.1 and phase  $\phi_s$ , between 0 and  $2\pi$  in steps of  $10^\circ$ . Radiation patterns and the corresponding radiated power are calculated by superimposing the scaled far fields emitted by the antenna, independently driven with nonlinear sources at two interfaces (see Eq. (6)).

Examining the radiation patterns at different regions of the complex  $s$  plane (as in the main text Fig. 3b,c), it becomes obvious that only radiation patterns simulated for values of  $s$  in a small part of the first quadrant resemble the experimentally observed ones, i.e. having a characteristic asymmetry along the short axis of the asymmetric-gap antenna (see Fig. 3b,d main text). By analyzing the detailed shape of the radiation patterns as well as the relative magnitudes of the intensities of long and short axis patterns for both asymmetric-gap and symmetric-gap antenna, one can single out the best fitting patterns for a limited set of points in the complex plane, the position of these points are denoted with red x's in Fig. S5a.

This set of optimal values for scaling parameters  $S = \{s_1, s_2, \dots\}$  is now used as a set of possible values for fitting of the power curves which is done as shown in Fig. S5b. Distances  $d_{Si}, d_{Ai}$  (where distance is defined as  $d = |P_{SH,e} - P_{SH,s}|$ , indices e and s denote experiment and simulation, respectively) between experimentally obtained normalized SH signals and corresponding simulated ones, for both asymmetric-gap (index A) and symmetric-gap (index S) antenna, are retrieved and summed up, yielding a total distance  $d = \sum(d_{Ai} + d_{Si})$ . The distance is minimized to retrieve an optimal value for the scaling parameter  $s$ . Since both experimental and simulated data are normalized to the equivalent reference SH signal (symmetric  $80^\circ$ ) and due to uncertainty in the experimental result, we introduce a scaling factor  $\sigma$  for the simulated curves. We can see in Fig. S5c that the minimum in distance between experiment and simulation, depending on the scaling factor  $\sigma$ , is reached for a value  $\sigma = 0.9$ . There, the optimal scaling parameter  $s$  for fitting both radiation patterns as well as SH power as a function of the tip opening angle data, has a value of 0.55 in amplitude and a phase of  $50^\circ$  ( $= 5/18\pi$  radians).

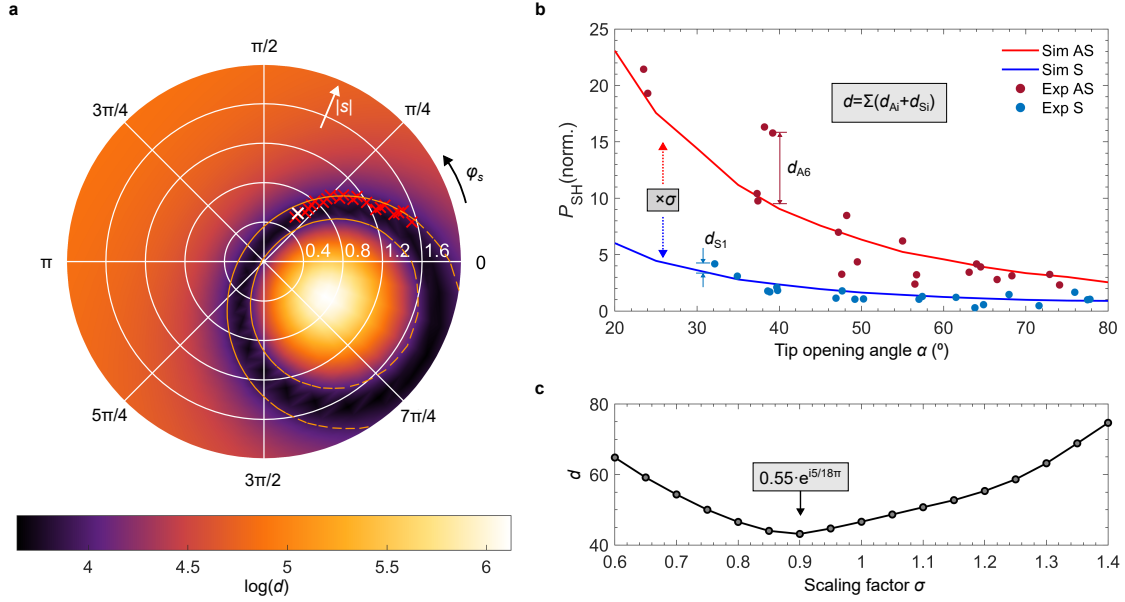


FIG. S5: **Finding the optimal  $s$  parameter.** **a**, Complex plane plot. Locations of optimal radiation patterns are denoted with red x markers, on top of the color plot showing the dependence of the logarithm of total distance  $d$  between experiment and simulation (power curves) on the scaling parameter  $s$  (position in the complex plane). The optimum of the scaling parameter is marked by a white x. **b**, Normalized SH power depending on the tip opening angle  $\alpha$  for simulation (solid line) and experiment (scattered data) for asymmetric-gap (red) and symmetric-gap (blue) antennas. For each of the experimental data points, the distance is calculated from the corresponding simulated curve. The total distance  $d$  is the sum of individual distances  $d_i$  and serves as a minimization parameter for fitting. **c**, Simulated curves are scaled with factor  $\sigma$  due to uncertainty in the experimentally obtained data. The minimum in distance is obtained for a scaling factor of 0.9.

### 1.5 Semi-analytical calculation of radiation patterns - effective dipole model

In this section we demonstrate how the radiation pattern of an arbitrary radiating system placed above a planar interface can be calculated by employing a semi-analytical approach (similar to [15]). Two main ingredients have to be considered, namely the total near-field polarization  $\mathbf{P}(\mathbf{r}_0)$  (in the text below it will be referred to as “source”), and far-field Green’s tensor of a point dipole  $\vec{\mathbf{G}}(\mathbf{r}, \mathbf{r}_0)$  for the geometry under consideration (here a planar interface between two half spaces). Here,  $\mathbf{r}_0 = (x_0, y_0, z_0)$  is position of a point source located above the planar interface, while the field is evaluated at a far-zone point  $\mathbf{r} = (x, y, z)$ . The electric field in the far-field  $\mathbf{E}(\mathbf{r})$  can be calculated using Eq. (5), where the total polarization  $\mathbf{P}(\mathbf{r}_0)$  is used instead of a nonlinear source polarization  $\mathbf{P}_S(\mathbf{r}_0)$ .

We separate the Green’s tensor into a part which solely depends on the position in the far-field and a scalar function  $f(\mathbf{r}, \mathbf{r}_0)$  which carries information of the position of the source in the near-field  $\vec{\mathbf{G}}(\mathbf{r}, \mathbf{r}_0) = f(\mathbf{r}, \mathbf{r}_0) \vec{\mathbf{G}}(\mathbf{r})$ . This allows us to take the tensor out of the integral and to simplify the calculation. The scalar function  $f$  is defined as

$$f(\mathbf{r}, \mathbf{r}_0) = \exp \left[ -ik_1 \left( x_0 \frac{x}{r} + y_0 \frac{y}{r} - z_0 \sqrt{1 - \left( \frac{n_2 \rho}{n_1 r} \right)^2} \right) \right], \quad (8)$$

where  $k_1$  is a wavevector in the upper half-space, while  $n_1, n_2$  are refractive indices of the upper and lower half-space, respectively.

The integration in Eq. (5) is performed over the volume  $V_0$  of the radiating system. In the most general case one can perform the integration and calculate the radiation pattern, however, at the cost of losing the physical picture behind the process. Since our source is mostly localized within the tip and in order to resolve the aforementioned problem, we can perform a Taylor expansion of the scalar function  $f$  and analyze the

contribution from each term separately – the expansion is performed around the center of mass of polarization  $\mathbf{r}_{\text{cm}}$  to minimize the error in the first term

$$f(\mathbf{r}, \mathbf{r}_0) = f(\mathbf{r}, \mathbf{r}_{\text{cm}}) + \Delta \mathbf{r}_0^T \nabla f(\mathbf{r}, \mathbf{r}_{\text{cm}}) + \frac{1}{2} \Delta \mathbf{r}_0^T \left[ \nabla \nabla^T f(\mathbf{r}, \mathbf{r}_{\text{cm}}) \right] \Delta \mathbf{r}_0 + \dots \quad (9)$$

Moreover, due to the form of the function  $f$ , none of the derivatives depend on the position in the near-field and can be taken out of the integral. Finally, the electric far-field can be calculated from the following expression:

$$\begin{aligned} \mathbf{E}(\mathbf{r}) = \frac{\omega^2 \mu_1}{\varepsilon_0 c^2} \overleftrightarrow{\mathbf{G}}(\mathbf{r}) \sum_i \{ & f(\mathbf{r}, \mathbf{r}_{\text{cm}}) \int_{V_0} \mathbf{P}_i(\mathbf{r}_0) dr_0^3 \\ & + \sum_j \partial_j f(\mathbf{r}, \mathbf{r}_{\text{cm}}) \int_{V_0} \Delta r_{0j} \mathbf{P}_i(\mathbf{r}_0) dr_0^3 \\ & + \frac{1}{2} \sum_{j,k} \partial_{jk} f(\mathbf{r}, \mathbf{r}_{\text{cm}}) \int_{V_0} \Delta r_{0j} \Delta r_{0k} \mathbf{P}_i(\mathbf{r}_0) dr_0^3 \\ & + \dots \}, \end{aligned} \quad (10)$$

where  $\mu_1$  denotes the relative permeability of the upper half-space medium and summations  $i, j, k$  run over the Cartesian components  $x, y, z$ . The first integral has only one term per component and is named effective dipole of a system. The second integral has three terms per component and corresponds to an effective quadrupole. The third integral has nine terms per component and is a measure of an octupole contribution of a system, and so on.

Due to symmetry of our structure and the excitation, an asymmetric-gap antenna will exhibit a strong effective dipole with zero  $y$ -component and non-zero  $x$ - and  $z$ -components. Moreover, since the effective dipole is the dominant term, shape and symmetry of the radiation pattern are already accurately represented by the first term of the Taylor expansion without the need of considering higher-order corrections, as shown in Fig. S6a. Nevertheless, by introducing both effective dipole and effective quadrupole (Fig. S6b), or even contributions up to the effective octupole (Fig. S6c), the obtained radiation patterns quickly converge to the full radiation patterns calculated with the Matlab toolbox (Fig. S6d).

In the case of symmetric-gap antennas, the effective dipole will, due to symmetry reasons, solely have a non-vanishing  $z$ -component, yielding a circular radiation pattern with intensity mostly localized around the critical angle. However, the symmetric-gap antenna exhibits rather strong, out-of-phase  $x$ -polarization in the two antenna arms. Therefore, the expectation is that non-negligible  $x$ -quadrupole terms should be obtained which implies spreading of the radiation pattern lobes in the  $x$ -direction (Fig. S6b). Other, higher-order contributions hardly affect the shape of the radiation pattern (Fig. S6c).

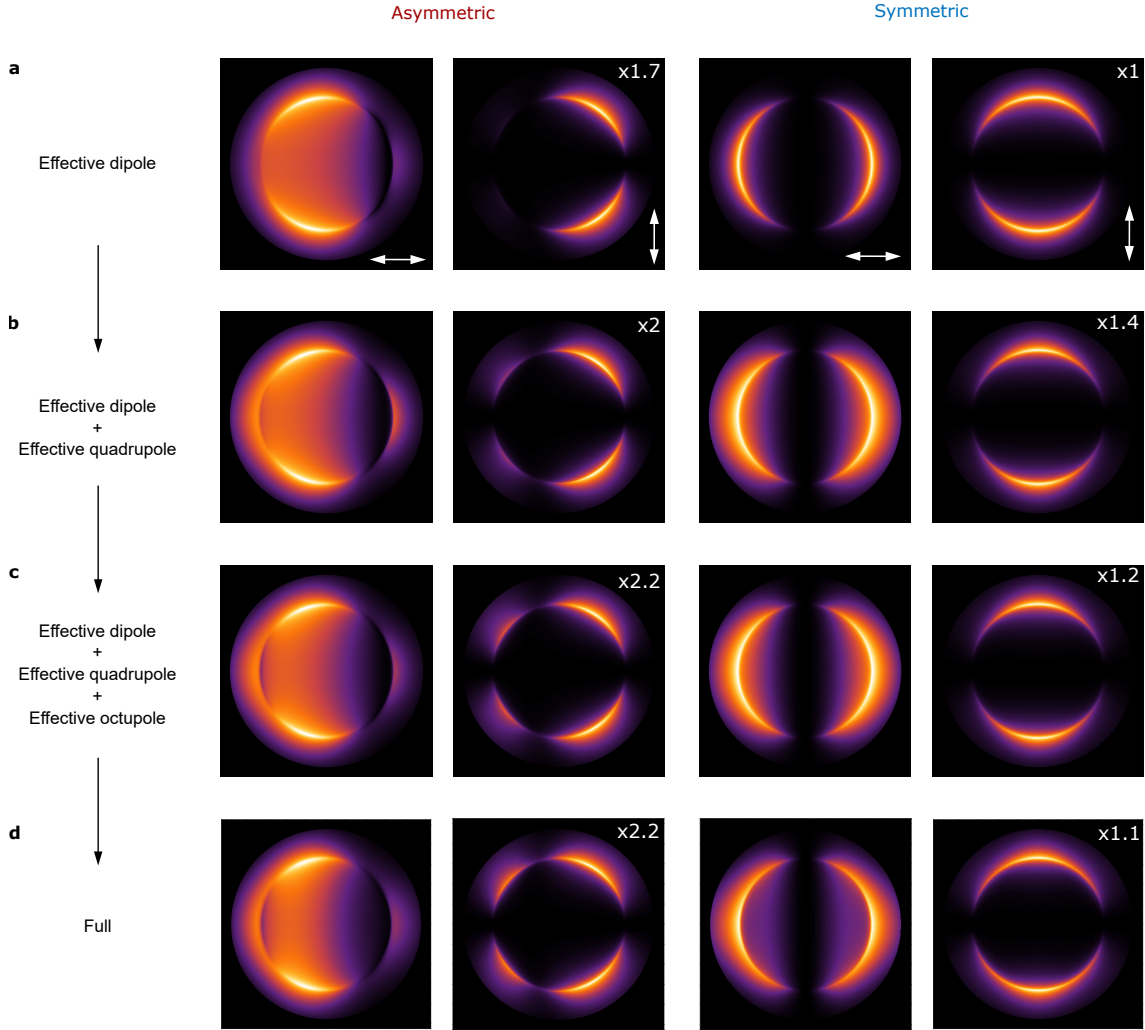


FIG. S6: **Semi-analytical calculation of radiation patterns.** Calculations for asymmetric-gap (two left columns) and symmetric-gap antenna (two right columns). **a-c**, Calculations are performed using the semi-analytical approach considering one, two and three orders of Eq. (10), respectively. **d**, Radiation patterns calculated using Matlab toolbox (RETOP 8.1), which is equivalent to summing all the terms of the semi-analytical approach.



## 2 Experiments

### 2.1 Fabrication

All antennas discussed in the main text are fabricated using a three-step milling method based on Ga-FIB and He-FIB milling. First, a Ga-ion beam with a current of 10 pA (acceleration voltage  $V_a = 30$  kV) is used to define the coarse shape of the antenna centered in a  $(4 \times 4) \mu\text{m}$  milled glass window to avoid unwanted reflections from the surrounding gold during optical measurements, see Fig. S7a. Subsequently, the exact antenna shape is defined by a He-ion beam ( $V_a = 35$  kV) with a current of 3.5 pA (Fig. S7b). For milling the gap, we reduce the He-ion beam current down to 1.5 pA (Fig. S7c) to achieve controlled gap sizes and gold tips with a minimal radius of curvature.

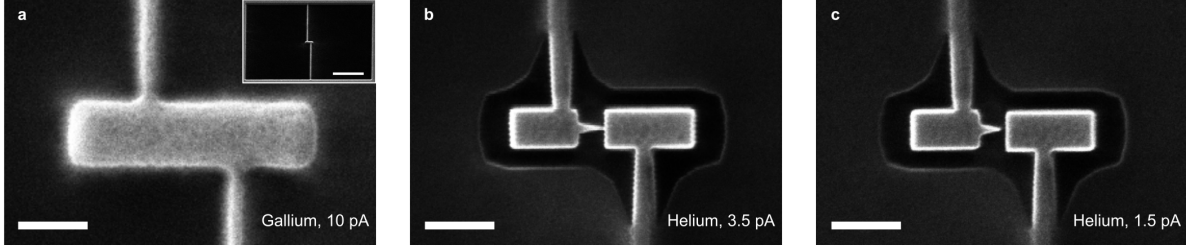


FIG. S7: **Helium ion microscope images illustrating the three-step milling approach based on Ga-/He-FIB.** Antenna after Ga-FIB **a**, first **b**, and second **c**, He-FIB step. Scale bars, 100 nm. The inset in **a** shows an overview of the antenna and the surrounding  $(4 \times 4) \mu\text{m}$  glass window. Scale bar, 1  $\mu\text{m}$ .

### 2.2 Optical setup for SHG measurements

Fig. S8 shows a scheme of the optical setup used for recording SHG spectra and radiation patterns. Broadening of the 100 fs laser pulse due to dispersion is precompensated by a single-prism pulse compressor before the objective. Design details can be found in Ref. [16]. To record radiation patterns, we place a 1000-mm Betrand lens in front of the spectrometer (at the position of the dashed line in Fig. S8) and replace the spectrometer grating by a mirror.

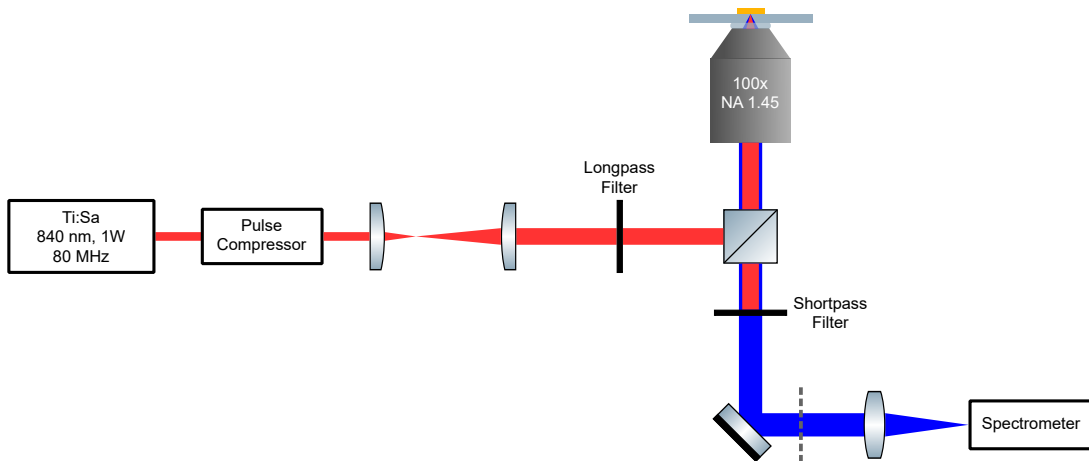


FIG. S8: **Scheme of the optical setup.** The beam of a Ti:Sa laser is focused onto the sample with a high NA objective (100 $\times$ , NA = 1.45, Nikon). A pulse compressor after the laser output is used to precompensate dispersion. The SH scattered light is analyzed using a spectrometer equipped with an EMCCD (see Methods in main text for details about manufacturers).

### 2.3 Linear properties

In Fig. S9 we show the single measurements of the angle-dependent SH power from Fig. 4 in the main text, including the information about the bonding mode resonance at the FF (circles correspond to asymmetric-gap, squares to symmetric-gap antennas, respectively). We compare the strength of the scattering amplitude at the resonance,  $A_{\text{scatt}}(\lambda_{\text{res}})$ , to the strength of the scattering amplitude at the excitation wavelength of 840 nm,  $A_{\text{scatt}}(840 \text{ nm})$ . To ensure comparability, we only take into account antennas where the resonance is equal or close to 840 nm, i.e.  $A_{\text{scatt}}(840 \text{ nm})/A_{\text{scatt}}(\lambda_{\text{res}}) > 0.9$ . Within this range we do not observe any dependence of the SH signal on the resonance position.

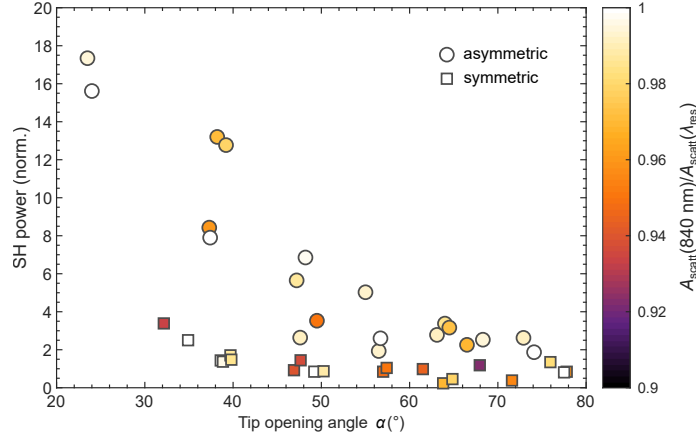
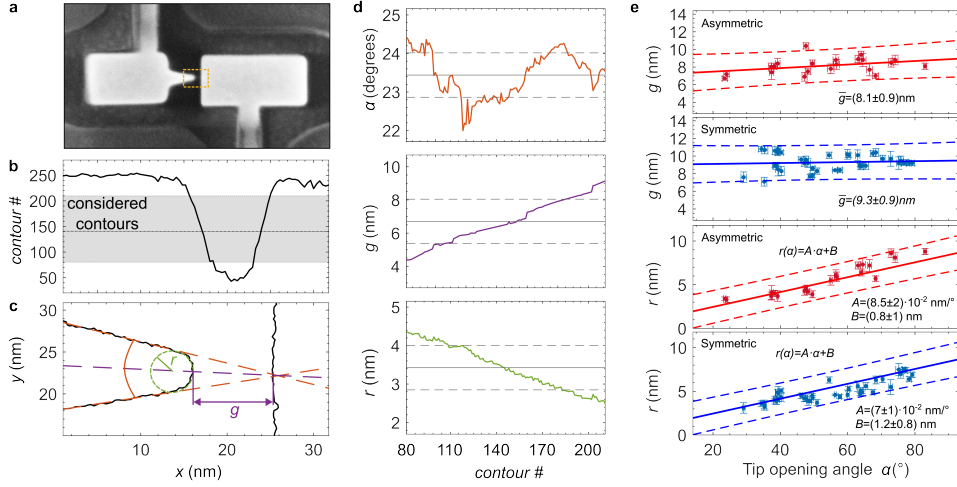


FIG. S9: **Analysis of the linear bonding mode resonance.** Raw data of the angle-dependent SH power shown in Fig. 4 in the main text. The color code indicates the deviation of the scattering amplitude at the antenna resonance,  $A_{\text{scatt}}(\lambda_{\text{res}})$ , from the scattering amplitude at 840 nm,  $A_{\text{scatt}}(840 \text{ nm})$ . Circles correspond to asymmetric-gap, squares to symmetric-gap antennas, respectively.

### 2.4 Antenna geometry

The antenna geometry determines the strength of the linear response (field enhancement) and in turn the strength of SH sources. Therefore, a detailed analysis of the geometry is needed to properly model the SH response of the system. To this end we analyse SEM images to obtain lateral dimensions of the antenna (Fig. S10) and employ AFM measurements to retrieve information of the height of the gold antenna and the glass pedestal (Fig. S11). The lateral dimensions are most important in the gap region where the majority of the SH sources are generated (Fig. S10a). Two critical parameters which describe the gap region are the gap size  $g$  and the radius of curvature of the tip  $r$ . To determine these parameters systematically we have performed a contour analysis, where we first take the line scan across the gap of the SEM image (Fig. S10b) and consider contours which are within the shaded region (contours too close to the top surface of antenna or substrate become discontinuous along the edge and are therefore disregarded). For each of the selected contours we fit the dashed orange lines to the tip side in order to determine the tip opening angle, as well as the green circle into the tip apex to obtain the radius of curvature (Fig. S10c). The gap size is determined from the distance of the points where the angle bisector (the purple dashed line) crosses the two contours (tip contour and straight edge contour). By doing so for each of the contours of interest, we obtain statistics of the different tip opening angles, gap sizes and radii of curvature for a single structure providing us with a tool to systematically determine the geometry of the gap region (Fig. S10d). Performing this for all of the structures under consideration we see that there is a tip opening angle dependent trend for gap size and radius of curvature which is different for the two types of antennas (Fig. S10e). The upper two rows in Fig. S10e denote the angle-dependent gap size for asymmetric-gap (red) and symmetric-gap (blue) structures. For different tip opening angles the gap size stays more or less constant with an average of  $(8.1 \pm 0.9) \text{ nm}$  for asymmetric-gap and  $(9.3 \pm 0.9) \text{ nm}$  for symmetric-gap antennas. On the other hand, in the bottom two rows of Fig. S10 we can see that the radius of curvature is decreasing





**FIG. S10: Contour analysis of SEM images.** **a**, SEM image of an exemplary asymmetric-gap antenna. The yellow square denotes the gap region which is analyzed. **b**, Line profile taken in the middle of the gap. Gray region denotes contours considered for the analysis. **c**, Exemplary contours marked with dotted black line **b**. Orange lines are fitted to the tip side to determine the opening angle. The green circle is fitted to the apex of the tip and is used to determine the radius of curvature. From the crossing of the angle bisector (dashed purple line) with the contours from the left and the right side, the gap size is determined. **d**, Tip opening angle  $\alpha$  (top), gap size  $g$  (middle) and radius of curvature  $r$  (bottom) depending on contour number for the contours shown in **c**. **e**, Dependence of gap size  $g$  (top two plots) and radius of curvature  $r$  (bottom two plots) on the tip opening angle for all asymmetric-gap (red) and symmetric-gap (blue) antennas shown in Fig. 4 in the main text.

from approximately 8 nm to 3 nm as the tip opening angle is reduced from  $80^\circ$  to  $20^\circ$ . This significant decrease in radius of curvature has a strong influence on the SH signal and is therefore implemented into the numerical model using the linear fit as presented in Fig. S10e.

The height of the antenna and pedestal do not play a critical role in the strength of the field enhancement in the gap, but still influence the spectral position of the bright mode at FF. We therefore also perform AFM topography measurements to retrieve information of the height of antenna and pedestal. In Fig. S11a and b we show an AFM topography of an exemplary antenna (no gap included) and the corresponding height profile, respectively. We obtain a total pedestal height of 50 nm originating from Ga- and He-FIB. We verify this result by He-milling simple rectangular patterns with increasing doses (see Fig. S11c), where we can see a linear trend between pedestal height and ion dose (typical dose used in the fabrication process corresponds to  $1.1 \text{ C/cm}^2$ ).

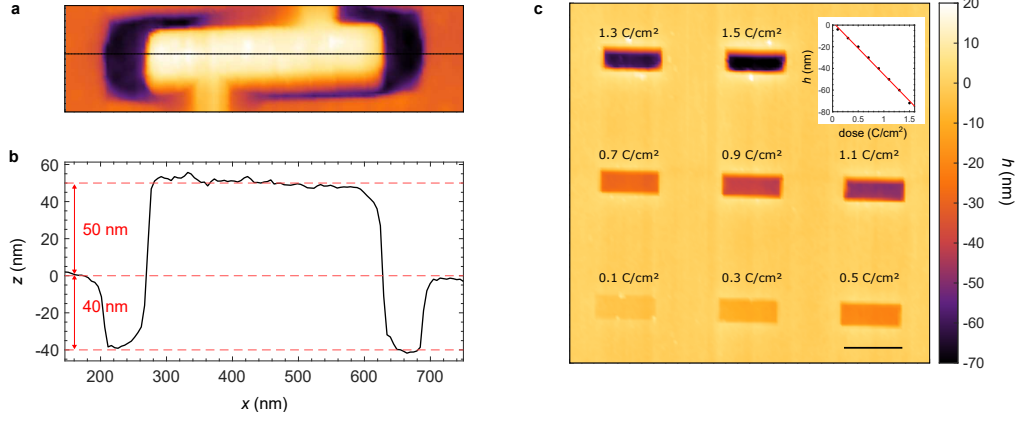


FIG. S11: **AFM measurements.** **a**, AFM topography of the antenna. **b**, Height profile recorded at the line in **a**. The height of antenna relative to the substrate after Ga- and He-FIB milling is 50 nm. From optical measurements we know that the gold platelet height is 40 nm. This implies 10 nm pedestal height produced during Ga-FIB milling. Fine milling using helium ions introduces additional 40 nm pedestal height. **c**, He-FIB depth depending on the used dose for exemplary rectangular patterns milled into a glass window created with Ga-FIB. Dose is increased from 0.1 up to 1.5 C/cm<sup>2</sup> in steps of 0.2 C/cm<sup>2</sup>.

## 2.5 Evaluation of efficiency

We evaluate the performance of our antennas similar to Ref. [17], see Table S1. To calculate the emitted photons per second at the SH, we have to take into account losses of the optical setup. Transfer functions of the single components, namely microscope objective, beam splitter, shortpass filter, mirrors, confocal lens, spectrometer mirror, grating, and EMCCD, are taken from the respective manufacturer data. Majority of SH radiation is emitted into the substrate half-space and we therefore assume a collection efficiency of 100% equivalent to Ref. [17]. Thus, for a wavelength of 420 nm we arrive at a detection efficiency of 0.04 resulting in  $9.9 \times 10^3$  emitted SH photons, evaluated for the asymmetric-gap antennas with  $\alpha = 25^\circ$  shown in Fig. 4 in the main text. Finally, for the maximum SH conversion efficiency we calculate  $\gamma_{\text{SH}} = 1.7 \times 10^{-10}$ . We want to emphasize that this is the same order of magnitude of what has been achieved in Ref. [17] ( $\gamma_{\text{SH}} = 5.1 \times 10^{-10}$ ), although we are working in the sub-500 nm wavelength regime, where gold exhibits strong damping, and the antennas do not exhibit a second resonance at the SH frequency.

Table S1: Efficiency calculation

<b>Parameter</b>	laser wavelength	laser rep. rate	laser pulse length	laser avg. power	NA objective	spot diameter	laser peak power
	$\lambda_{\text{exc}}$	$f_{\text{rep}}$	$\tau$	$P_{\text{avg}}$		$\delta$	$P_{\text{peak}}$
<b>Unit</b>	nm	MHz	fs	$\mu\text{W}$		$\mu\text{m}$	W
<b>Formula</b>						$1.22\lambda/\text{NA}$	$P_{\text{avg}}/(f_{\text{rep}}\tau)$
<b>Value</b>	840	80	100	15	1.45	0.707	1.9
<b>Parameter</b>	em. SH photons	SH power	SH peak power	max. SH conv. efficiency	peak nonlinear coefficient $\gamma_{\text{SH}}$		
	$N$	$P_{\text{SH}}$	$P_{\text{SH, peak}}$	$\eta_{\text{SH}}$			
<b>Unit</b>	cts/s	W	W		W <sup>-1</sup>		
<b>Formula</b>		$N \cdot E_{\text{ph}}$	$P_{\text{SH}}/(f_{\text{rep}}\tau)$	$P_{\text{SH}}/P_{\text{avg}}$	$P_{\text{SH, peak}}/(P_{\text{peak}})^2$		
<b>Value</b>	$9.9 \times 10^3$	$4.7 \times 10^{-15}$	$5.9 \times 10^{-10}$	$3.1 \times 10^{-10}$	$1.7 \times 10^{-10}$		

## References

- [1] COMSOL Multiphysics® v. 6.0. [www.comsol.com](http://www.comsol.com). COMSOL AB, Stockholm, Sweden.
- [2] Swen Großmann, Daniel Friedrich, Michael Karolak, René Kulloock, Enno Krauss, Monika Emmerling, Giorgio Sangiovanni, and Bert Hecht. Nonclassical optical properties of mesoscopic gold. *Physical Review Letters*, 122(24):246802, 2019.
- [3] Schott AG. Schott glass data sheets, 2017.
- [4] Robert L Olmon, Brian Slovick, Timothy W Johnson, David Shelton, Sang-Hyun Oh, Glenn D Boreman, and Markus B Raschke. Optical dielectric function of gold. *Physical Review B*, 86(23):235147, 2012.
- [5] Fu Xiang Wang, Francisco J Rodríguez, Willem M Albers, Risto Ahorinta, JE Sipe, and Martti Kauranen. Surface and bulk contributions to the second-order nonlinear optical response of a gold film. *Physical Review B*, 80(23):233402, 2009.
- [6] JE Sipe, VCY So, M Fukui, and GI Stegeman. Analysis of second-harmonic generation at metal surfaces. *Physical Review B*, 21(10):4389, 1980.
- [7] K Nireekshan Reddy, Parry Y Chen, Antonio I Fernández-Domínguez, and Yonatan Sivan. Revisiting the boundary conditions for second-harmonic generation at metal-dielectric interfaces. *JOSA B*, 34(9):1824–1832, 2017.
- [8] Yi Yang, Di Zhu, Wei Yan, Akshay Agarwal, Mengjie Zheng, John D Joannopoulos, Philippe Lalanne, Thomas Christensen, Karl K Berggren, and Marin Soljačić. A general theoretical and experimental framework for nanoscale electromagnetism. *Nature*, 576(7786):248–252, 2019.
- [9] Fan Yang and Cristian Ciraci. Second-harmonic generation from singular metasurfaces. *Phys. Rev. B*, 105:235432, Jun 2022.
- [10] Kevin O’Brien, Haim Suchowski, Junsuk Rho, Alessandro Salandrino, Boubacar Kante, Xiaobo Yin, and Xiang Zhang. Predicting nonlinear properties of metamaterials from the linear response. *Nature materials*, 14(4):379–383, 2015.
- [11] Jianji Yang, Jean-Paul Hugonin, and Philippe Lalanne. Near-to-far field transformations for radiative and guided waves. *ACS photonics*, 3(3):395–402, 2016.
- [12] A Benedetti, M Centini, C Sabilia, and M Bertolotti. Engineering the second harmonic generation pattern from coupled gold nanowires. *JOSA B*, 27(3):408–416, 2010.
- [13] Maria Antonietta Vincenti, Salvatore Campione, Domenico de Ceglia, Filippo Capolino, and Michael Scalora. Gain-assisted harmonic generation in near-zero permittivity metamaterials made of plasmonic nanoshells. *New Journal of Physics*, 14(10):103016, 2012.
- [14] Lukas Novotny and Bert Hecht. *Principles of nano-optics*. Cambridge university press, 2012.
- [15] Alexandre Bouhelier, M Beversluis, Achim Hartschuh, and Lukas Novotny. Near-field second-harmonic generation induced by local field enhancement. *Physical review letters*, 90(1):013903, 2003.
- [16] Selcuk Akturk, Xun Gu, Mark Kimmel, and Rick Trebino. Extremely simple single-prism ultrashort-pulse compressor. *Optics Express*, 14(21):10101, 2006.
- [17] Michele Celebrano, Xiaofei Wu, Milena Baselli, Swen Großmann, Paolo Biagioni, Andrea Locatelli, Costantino De Angelis, Giulio Cerullo, Roberto Osellame, Bert Hecht, Lamberto Duò, Franco Ciccacci, and Marco Finazzi. Mode matching in multiresonant plasmonic nanoantennas for enhanced second harmonic generation. *Nature Nanotechnology*, 10(5):412–417, 2015.